

1
2
3 **Influence of Mineral Composition of Chars Derived by Hydrothermal Carbonization**
4
5 **on Sorption Behavior of CO₂, CH₄ and O₂**
6
7
8
9

10 Carsten Wedler¹, Katrin Lotz², Arash Arami-Niya^{3,4}, Gongkui Xiao³, Roland Span¹,
11
12 Martin Muhler², Eric F. May³, Markus Richter^{3,5,*}
13
14

15
16
17 ¹ *Thermodynamics, Ruhr University Bochum, 44780 Bochum, Germany*

18
19 ² *Laboratory of Industrial Chemistry, Ruhr University Bochum, 44780 Bochum, Germany*

20
21 ³ *Fluid Science & Resources Division, Department of Chemical Engineering, The University of*
22
23 *Western Australia, Perth, WA 6009, Australia*

24
25 ⁴ *Discipline of Chemical Engineering, Western Australian School of Mines: Minerals, Energy and*
26
27 *Chemical Engineering, Curtin University, Perth, WA 6845, Australia*

28
29 ⁵ *Applied Thermodynamics, Chemnitz University of Technology, 09126 Chemnitz, Germany*
30
31
32
33

34 **ABSTRACT**

35
36
37 The doping of SiO₂ and Fe₂O₃ into hydrochars that were produced by the hydrothermal
38 carbonization of cellulose was studied with respect to its impact on the resulting surface
39 characteristics and sorption behavior of CO₂, CH₄ and O₂. During pyrolysis, the structural order
40 of the Fe-doped char changed, as the fraction of highly ordered domains increased, which was
41 not observed for the undoped and the Si-doped chars. The Si-doping had no apparent influence
42 on the oxidation temperature of the hydrochar in contrast to the Fe-doped char where the
43 oxidation temperature was reduced because of the catalytic effect of Fe. Both dopants reduced
44 the micro-, meso- and macroporous surface areas of the chars, although the Fe-doped chars had
45 larger meso- and macroporosity than the Si-doped char. However, the increased degree in
46
47
48
49
50
51
52
53
54
55
56
57
58
59
60

* Corresponding author. Tel.: +49-371-531-38050, E-mail: m.richter@mb.tu-chemnitz.de

1
2
3 structural order of the carbon matrix of the Fe-doped char reduced its microporosity relative to
4 the Si-doped char. The adsorption of CO₂ and CH₄ on the chars at temperatures between
5 273.15 K and 423.15 K and at pressures up to 115 kPa was slightly inhibited by the Si-doping
6 but strongly suppressed by the Fe-doping. For O₂, however, the Si-doping promoted the
7 observed adsorption capacity, while Fe-doping also showed an inhibiting effect.
8
9
10
11
12
13
14
15
16
17
18
19
20
21
22
23
24
25
26
27
28
29
30
31
32
33
34
35
36
37
38
39
40
41
42
43
44
45
46
47
48
49
50
51
52
53
54
55
56
57
58
59
60

1. INTRODUCTION

HTC chars, which are pyrolyzed hydrochars derived via hydrothermal carbonization (HTC) under high pressure from lignocellulosic biomass and water, have aroused interest in many fields of science and application over recent years.¹ One promising research focus is the use of hydrochars as a fuel in biomass-fired power generation or as a possible substitute in coal-fired power plants^{2,3} because such an application could help meet increasing global energy demand while reducing associated CO₂ emissions. After pyrolysis, the resulting HTC chars possess large surface areas, which makes them also a promising adsorbent material for subsequent use in the removal of environmental pollutants from flue gases or waste water.⁴

The elemental composition of solid biofuels can differ a lot. Depending on different raw plants, woods or agricultural wastes, the mineral content of e.g. iron, silica or potassium can vary significantly, which can have a catalytic effect on morphology, pyrolysis, gasification and combustion.⁵⁻⁸ Trubetskaya et al.⁶ have shown for two biomasses with different silica and potassium content that the high silica content of rice husk leads to a preserved shape of the char particles during pyrolysis, whereby the low silica and high potassium content of wheat straw leads to a broader deviation of particle shape. The higher potassium content of the wheat straw also resulted in a higher reactivity of the char, which was also confirmed by various studies for different biomass.^{5,9,10} Khelifa et al.⁷ have shown the catalytic effect of Fe₂O₃ on pyrolysis and gasification of miscanthus chars. For these studies, the catalytic effect was shown through using different natural biomass with different mineral composition⁶, through the addition of further mineral particles to the biomass particles⁷ or through acid leaching of the most of the original mineral content with additional doping of the investigated mineral^{5,8-10}. Therefore, interactions between the different mineral components or influences of the acid leaching cannot be distinguished clearly.

1
2
3 Due to the rudimental composition of the hydrochar derived via HTC from pure cellulose,
4 interactions between different minerals can be excluded. By doping minerals into the hydrochar
5 matrix, the nature and the arrangement of active sites on the surface of the char can be modified,
6 which leads to different combustion and adsorption properties. The doping of iron oxide into
7 the hydrochar results as well in a faster oxidation of the char due to the catalytic effects of
8 iron,¹¹⁻¹³ whereas the doping of silica does not show a significant effect on the oxidation rate.¹²
9
10 As diffusion and adsorption precede oxidation, this observation suggests that such doping might
11 similarly influence these mass transport mechanisms. Any differences in the diffusion and
12 adsorption of gas molecules in the porous structure of the char would also lead to changed
13 reaction rates during combustion and gasification given the importance of these mass
14 transport mechanisms to such reactions.¹⁴ Several studies investigated the adsorption behavior
15 of HTC chars, originating from different biomass materials such as different wood and
16 agricultural residues.¹⁵⁻¹⁹ Since the biomasses consist of various amounts of cellulose, minerals
17 and functional groups, a closer look on those components is here expedient as well. Very few
18 studies focusing on the influence of the mineral content or the functional groups of the
19 hydrochars on the adsorption properties have been carried out. Yu *et al.* investigated the
20 influence of the iron content of hydrochars on the removal of estrogen and Lei *et al.* studied the
21 influence of the nitrogen-containing functional groups on the removal of chromium, both from
22 waste water.^{20,21} To the best of our knowledge, no study exists on the influence of the iron or
23 silica content on the adsorption of CO₂, CH₄ or O₂.

24
25
26 Therefore, a novel approach about the influence of iron and silica doping on the adsorption
27 behavior of CO₂, CH₄ and O₂ is presented in this study, followed by a comprehensive estimation
28 of the volumetric adsorption measurement uncertainty. Changes in morphology and amount of
29 active surface sites due to mineral doping and pyrolysis of the hydrochars lead to different
30 adsorption behavior of the chars. Since the adsorbed phase is a precursor for the following solid-

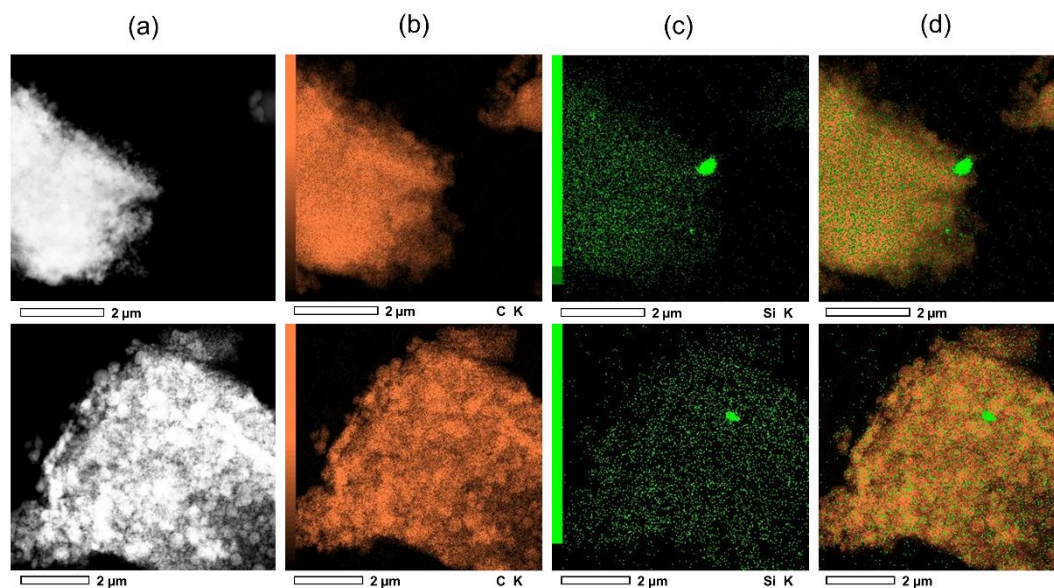
1
2
3 gas interactions during pyrolysis, gasification and combustion, the investigation of the influence
4
5 of the mineral composition leads to a better understanding of the process.
6
7

8 **2. RESULTS AND DISCUSSION**

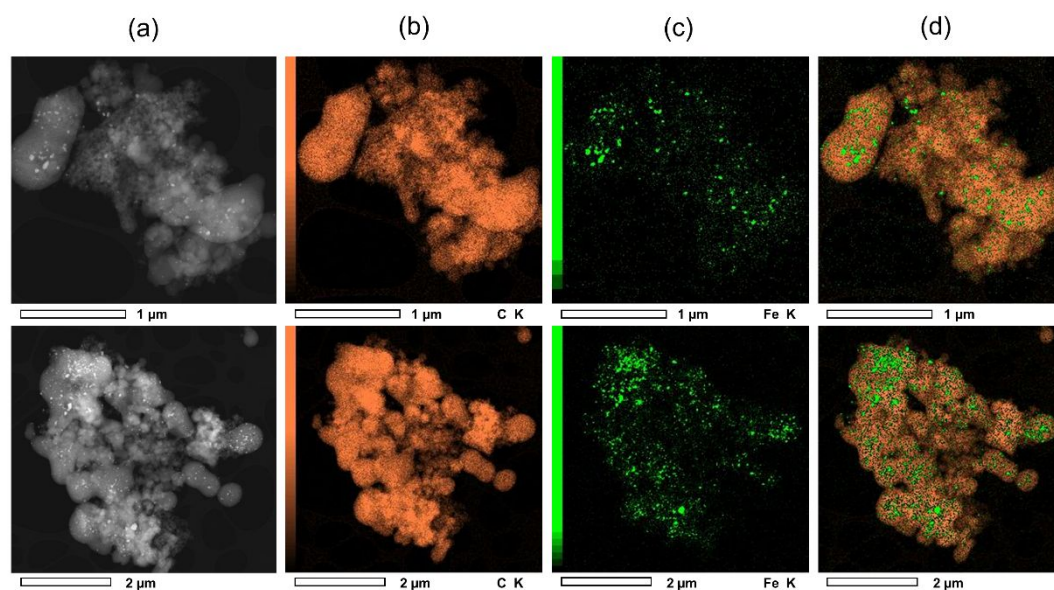
9 **2.1. Characterization of the HTC chars**

10 **2.1.1. Elemental mapping**

11
12
13 Electron microscopy imaging and energy-dispersive elemental mapping of the doped HTC
14
15 chars were performed to obtain information about the mode of incorporation of the dopants and
16
17 are presented in Figure 1 and Figure 2. According to the micrographs, the particles consist of
18
19 agglomerates of spheres differing in size. Elemental mapping of the Si-doped (see Figure 1 b-d)
20
21 and the Fe-doped (see Figure 2 b-d) HTC char reveals that the dopant particles are in immediate
22
23 vicinity of the carbonaceous spheres. Thus, we assume that the dopant particles are incorporated
24
25 in the hydrochar during the hydrothermal carbonization process and remain in contact to the
26
27 char matrix after pyrolysis. For the Fe-doped char, elemental mapping shows a higher
28
29 dispersion of the dopant in the char, which is presumably due to the lower particle size of the
30
31 added Fe₂O₃ particles compared with those for SiO₂.
32
33
34
35
36
37
38
39
40
41
42
43
44
45
46
47
48
49
50
51
52
53
54
55
56
57
58
59
60



23 **Figure 1.** STEM micrograph (a) as well as elemental mapping with respect to carbon (b) and
24 silicon (c) for two different particles of the Si-doped char. The overlay (d) is based on the
25 individual distributions of carbon and silicon.
26



47 **Figure 2.** STEM micrograph (a) as well as elemental mapping with respect to carbon (b) and
48 iron (c) for two different particles of the Fe-doped char. The overlay (d) is based on the
49 individual distributions of carbon and iron.
50

51 2.1.2. X-ray diffraction

52
53
54 To identify the phases of organic and inorganic matter in the HTC chars, XRD patterns were
55 recorded and are shown in Figure 3. Also shown are the peak locations corresponding to the
56 reference patterns of graphite, quartz, iron and cohenite.
57
58
59
60

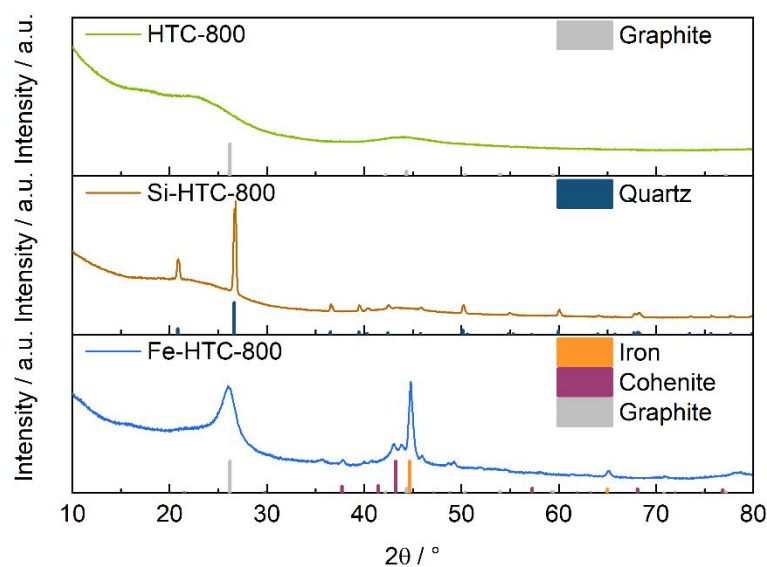


Figure 3. XRD patterns of the undoped (HTC-800), the Si-doped (Si-HTC-800) and the Fe-doped (Fe-HTC-800) HTC char (Reference patterns: Graphite: 01-075-1621; SiO₂: 01-070-7344; Fe⁰: 03-065-4899; Fe₃C: 01-089-2005).

In the XRD pattern of the undoped char, no sharp reflections can be observed in the range $2\theta = 10^\circ$ to 80° , suggesting that this carbon material is X-ray amorphous. TEM imaging of the char verifies a low degree of structural order (see Figure S1 in supporting information). Thus, pyrolysis up to $T = 1073$ K does not generate a high fraction of highly ordered domains in the undoped HTC char. The XRD pattern of the Si-doped HTC char contains several sharp reflections, which can be assigned to Quartz (SiO₂). This indicates that the dopant maintains its phase composition during the hydrothermal synthesis and the subsequent pyrolysis. In contrast, a phase transition occurs for the Fe-doped char: carbothermal reduction of the Fe₂O₃ dopant during the thermal treatment results in metallic iron (Fe⁰) and iron carbide (Fe₃C) as revealed by the detail investigations shown previously.²² This is possibly accompanied by an increase in structural order of the carbonaceous matter as indicated by the reflection at $2\theta = 26^\circ$ referring to graphitic carbon. Given any structural order is much less pronounced for the undoped and the Si-doped char, the diffraction pattern and the TEM image (see Figure S1 in supporting information) reveal that the in situ addition of the iron dopant introduces structural order to the char by enabling far more highly ordered domains than observed in the other chars.

2.1.3. Surface area characteristics and pore size distribution

For all three HTC chars, the meso- to macroporous surface area was investigated by conducting a BET analysis of sorption isotherms measured for N_2 at $T = 77.36$ K (Figure 4). For all HTC chars, a pronounced increase in the amount of N_2 adsorbed is observed for very low relative pressures, which gives a first hint of the more microporous carbon structures. For p/p_0 in the range 0.1 and 0.8 the doped chars exhibit reduced adsorption capacity suggesting a low fraction of small mesopores relative to the undoped char. Stronger adsorption occurs as the saturation pressure is approached, with capillary condensation evident in large mesopores and macropores.

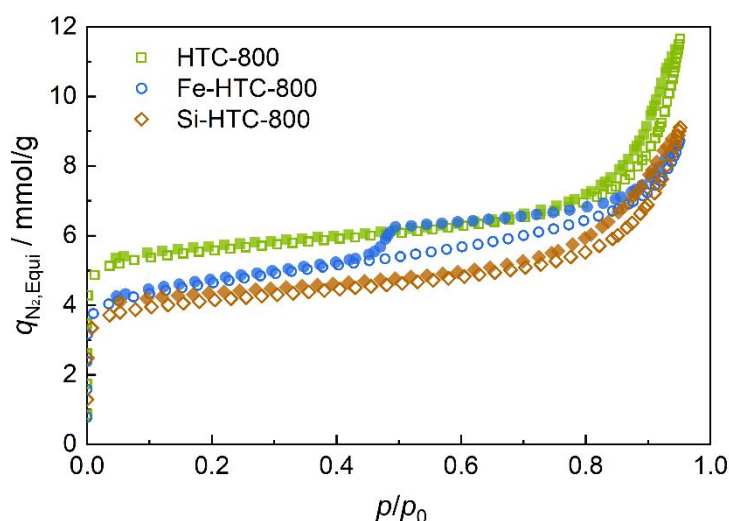


Figure 4. N_2 physisorption isotherms at 77.36 K of the undoped (HTC-800), the Si-doped (Si-HTC-800) and the Fe-doped (Fe-HTC-800) HTC chars. Hollow symbols correspond to adsorption data while filled symbols correspond to desorption data.

Although the shape of the sorption isotherms of the undoped and the Si-doped char are similar, the amount of N_2 adsorbed on the latter is significantly lower. This is reflected by the BET surface areas of the chars, which amounted to 416 m^2/g , 350 m^2/g and 310 m^2/g for the undoped, the Fe-doped and the Si-doped HTC char, respectively (see Table 1). In contrast to the undoped and the Si-doped chars, the adsorption and desorption isotherms of the Fe-doped char exhibit a more pronounced hysteresis. Based on previous studies,²² this feature is

presumably caused by the desorption of the adsorbate from cavities in the carbonaceous material produced by the structural changes occurring during pyrolysis. The increase for all three samples at very small pore sizes below 2 nm indicates a pronounced micropore structure.

Table 1. Comparison of surface areas of the undoped (HTC-800), the Si-doped (Si-HTC-800) and the Fe-doped (Fe-HTC-800) HTC chars determined by N₂ adsorption at $T = 77.36$ K (BET) and by CO₂ adsorption at $T = 273.15$ K (DA and BET).

	HTC-800	Si-HTC-800	Fe-HTC-800
$S_{N_2, BET}$ [m ² /g]	416	310	350
$S_{CO_2, DA}$ [m ² /g]	784	666	502
$S_{CO_2, BET}$ [m ² /g]	357	341	236

To investigate the micropore structure (< 2 nm), CO₂ adsorption isotherm data at $T = 273.15$ K (see Figure 7) were used to determine a micropore surface area of each char (see Table 1) via the Dubinin-Astakhov equation as extended by the equation of Medek.^{23,24} In general, the micropore surface area of all three chars is significantly larger than the BET surface area. We note that comparisons of the absolute values obtained from the models should be treated with caution, although differences in both $S_{N_2, BET}$ and $S_{CO_2, DA}$ are likely indicative of the HTC chars having different pore structures. The micropore surface area of the Si-doped char (666 m²/g) is much larger than that of the Fe-doped char (502 m²/g), which possibly reflects the reduction in microporosity caused by the generation of highly ordered domains induced by iron doping. In a few literature studies^{25,26} the BET theory has also been applied to the CO₂ isotherm data to calculate another estimate of the microporous surface area, $S_{CO_2, BET}$. This is done here and the results presented in Table 1 also indicate that the Fe-HTC-800 has the smallest surface area.

By conducting NLDFT calculations using the data from the initial slope of the N₂ adsorption isotherm, the pore size distribution (PSD) of the three chars for the micropore regime was calculated. For all three chars a regularization parameter $\lambda = 1.625$ was applied based on the optimized result of the L-curve for the Si-doped HTC char. For the undoped and the Si-doped char a bimodal distribution was obtained, with a sharp peak at around 0.4 nm for both, and a

broader peak at around 0.9 nm for the undoped and around 1.2 nm for the Si-doped char. Having in mind that N_2 is kinetically hindered at cryogenic temperatures to diffuse into the narrow micropores, the absolute values of the pore size distribution have to be considered carefully, but give at least a hint of the distribution of the micropores. The larger peak areas of the undoped char show a more pronounced microporous structure than that of the Si-doped chars. A unimodal distribution with a broad peak around 0.8 nm was obtained for the Fe-doped char, resulting in a less pronounced microporosity for the Fe-doped char. These observations confirm the results of the microporous surface area $S_{CO_2,DA}$. The unimodality also indicates a different structural order of the Fe-doped char as described in section 2.1.2.

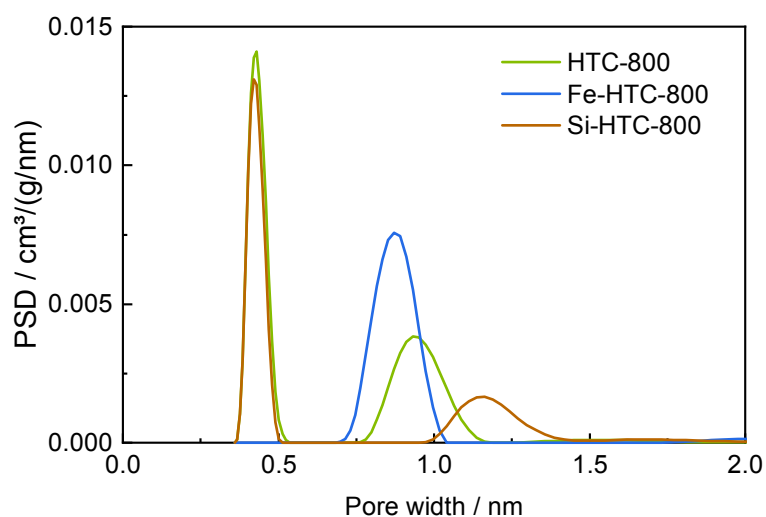


Figure 5. Pore size distributions obtained by NLDFT analysis of the undoped (HTC-800), the Si-doped (Si-HTC-800) and the Fe-doped (Fe-HTC-800) HTC char.

2.1.4. Oxidation behavior

The stability of the HTC chars can be determined by temperature-programmed oxidation (TPO) as the conversion of carbon materials by oxidation usually occurs at lower temperatures than required for gasification. The differential thermogravimetric (DTG) curves shown in Figure 6 were calculated by evaluating the first derivative of the sample mass changes measured during the TPO experiments.

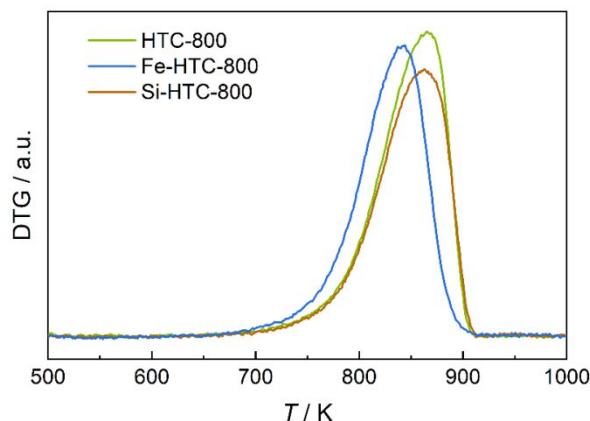


Figure 6. DTG curves during TPO in synthetic air in a thermobalance of the undoped (HTC-800), the Si-doped (Si-HTC-800) and the Fe-doped (Fe-HTC-800) HTC char.

The DTG profiles of the three HTC chars exhibit one broad signal in the temperature range between 673.15 K and 923.15 K corresponding to a single-step mass loss. The oxidation temperature corresponding to the maximum of the DTG peak was $T = 865.15$ K for the undoped char and was not affected by the addition of SiO_2 . The decreased height of the DTG signal obtained for the Si-doped char is caused by the lower relative fraction of oxidizable carbonaceous material present relative to that in the same initial amount of undoped char. Doping with iron produced a slight decrease of the char oxidation temperature, which can be attributed to a catalytic effect of the dopant. Nevertheless, the TPO and DTG data reveal that all three HTC chars are stable at the temperatures at which the sorption of CO_2 , CH_4 and O_2 were measured.

2.2. Sorption equilibria of CO_2 , CH_4 and O_2

The adsorption loadings of CO_2 on the three different chars were measured at five temperatures between 273.15 K and 423.15 K and are shown in Figure 7. For each temperature, similar trends can be observed. The largest CO_2 loadings were measured at 115 kPa for the undoped char (3.46 mmol/g at $T = 273.15$ K to 0.38 mmol/g at $T = 423.15$ K), followed by the Si-doped char (3.06 mmol/g at $T = 273.15$ K to 0.34 mmol/g at $T = 423.15$ K) and the Fe-doped char (2.24 mmol/g at $T = 273.15$ K to 0.24 mmol/g at $T = 423.15$ K).

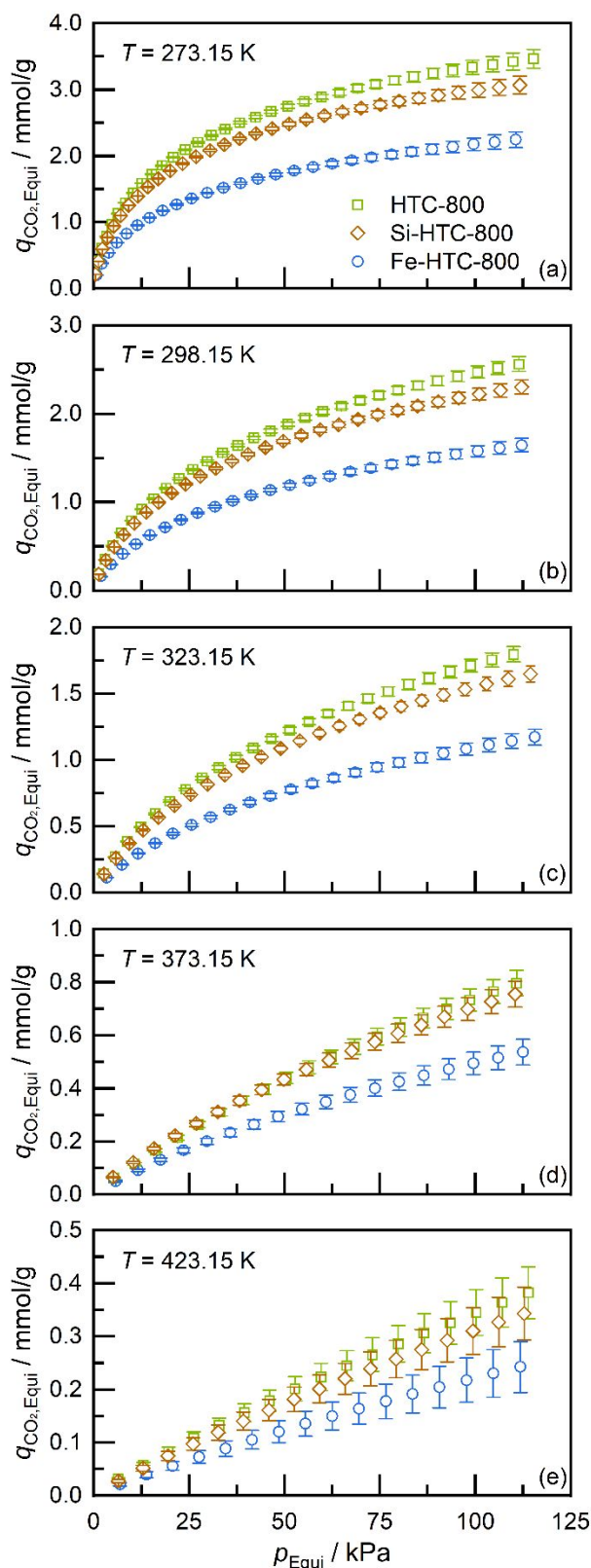


Figure 7. Adsorption loadings of CO_2 on the undoped (HTC-800), the Si-doped (Si-HTC-800) and the Fe-doped (Fe-HTC-800) HTC chars at different temperatures. (a) $T = 273.15 \text{ K}$; (b) $T = 298.15 \text{ K}$; (c) $T = 323.15 \text{ K}$; (d) $T = 373.15 \text{ K}$; (e) $T = 423.15 \text{ K}$. The isotherms for the undoped HTC char at $T = 273.15 \text{ K}$ and $T = 298.15 \text{ K}$ were reported previously.²⁷

1
2
3 The large adsorption loading of the undoped char can be explained by the fact it had the largest
4 BET surface area (416 m²/g) and/or as a result of the reduction in attractive forces between the
5 CO₂ and carbonaceous material caused by the doped minerals. However, the lower CO₂ loading
6 of the Fe-doped char relative to the Si-doped char cannot be related to their BET surface areas
7 of 350 m²/g and 310 m²/g, respectively. However, the different microporous pore structure of
8 the Fe-doped char (see section 2.1.3) resulting from the enhanced structural order likely
9 impedes the CO₂ adsorption process. A similar trend for the different chars was obtained for
10 the adsorption measurements with CH₄ at the four temperatures between 273.15 K and 373.15
11 K, although the adsorption loadings were considerably lower than for CO₂ (see Figure 8). At
12 1.80 mmol/g, 1.62 mmol/g and 1.15 mmol/g for the undoped, Si-doped and Fe-doped chars,
13 respectively, the resulting adsorption loadings at 115 kPa and 273.15 K are all about 48 % lower
14 than for CO₂. This trend simply reflects the generally lower adsorption affinity of CH₄ on any
15 material (see here for another example²⁸). The difference in adsorption loadings for the three
16 chars can also be explained in terms of the changes in microporosity resulting from the doping
17 process, since the adsorption of CH₄ is related to the microporosity as well.²⁹ However, a
18 directly inhibiting effect of the doped minerals is also possible.
19
20
21
22
23
24
25
26
27
28
29
30
31
32
33
34
35
36
37
38
39
40
41
42
43
44
45
46
47
48
49
50
51
52
53
54
55
56
57
58
59
60

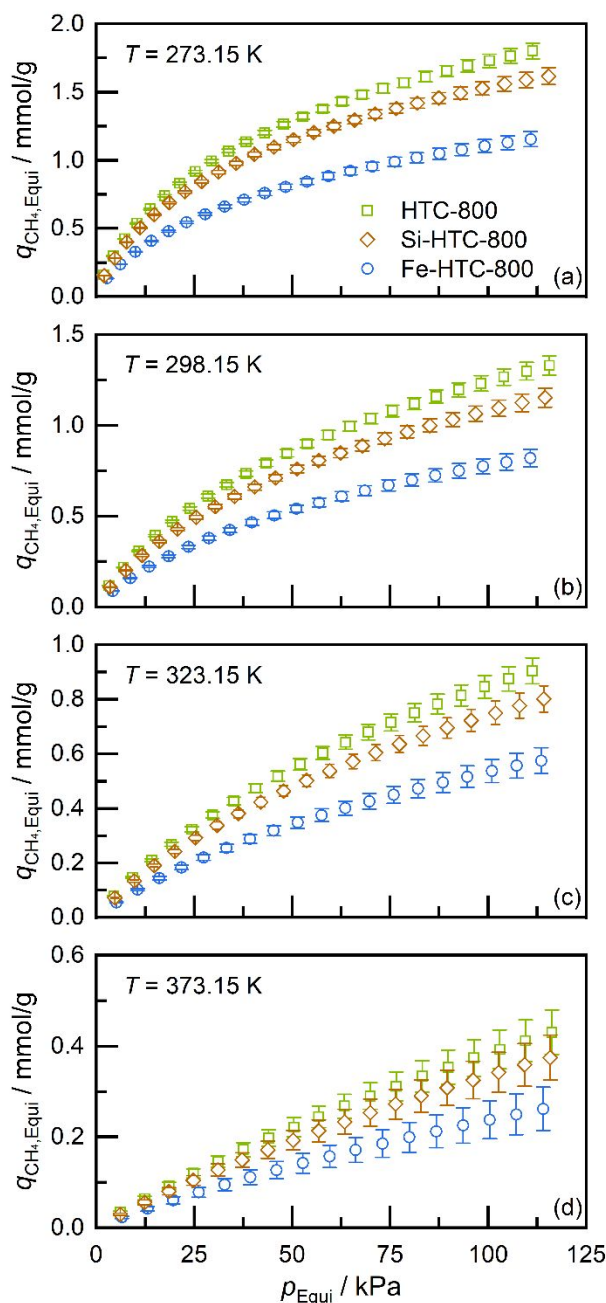
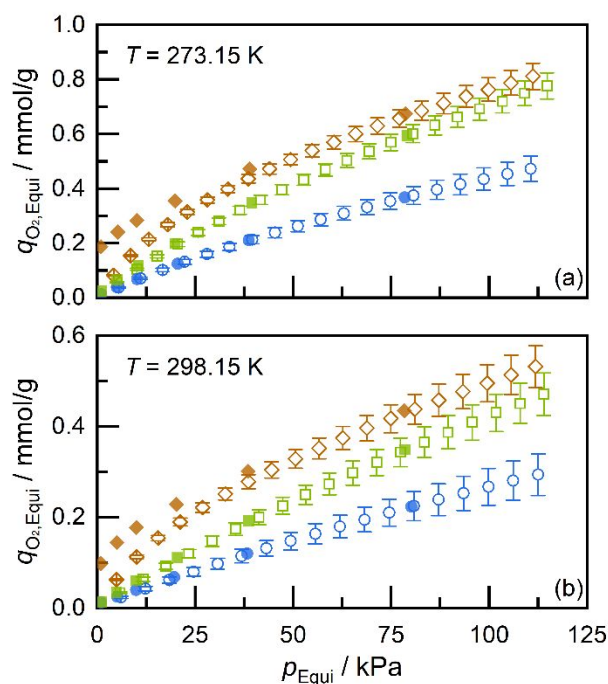


Figure 8. Adsorption loadings of CH_4 on the undoped (HTC-800), the Si-doped (Si-HTC-800) and the Fe-doped (Fe-HTC-800) HTC chars at different temperatures. (a) $T = 273.15 \text{ K}$; (b) $T = 298.15 \text{ K}$; (c) $T = 323.15 \text{ K}$; (d) $T = 373.15 \text{ K}$. The isotherms for the undoped HTC char at 273.15 K and 298.15 K were reported previously.²⁷

Figure 9 shows the adsorption of O_2 on the chars at $T = 273.15 \text{ K}$ and $T = 298.15 \text{ K}$, which exhibit a different trend than observed for CO_2 and CH_4 . At $T = 273.15 \text{ K}$, the largest O_2 loadings measured were for the Si-doped char (0.81 mmol/g), followed by the undoped char (0.78 mmol/g) and the Fe-doped char (0.47 mmol/g): this sequence cannot be explained by either the microporosity or the meso- to macroporosity of the samples. Furthermore, for the Si-

1
2
3 doped char, a repeatable desorption hysteresis was observed for the lowest pressures at both
4
5 temperatures, which indicates a behavior other than regular physisorption. To explain this
6
7 behavior it is helpful to consider the XRD patterns of the Si-doped char which show the
8
9 presence of quartz. At the temperature of the doping process of $T = 473.15$ K, the crystalline
10
11 structure of the doped SiO_2 is α -quartz.³⁰ Above a temperature of $T = 846$ K a displacive
12
13 transformation between α -quartz and β -quartz occurs, whereby one of the tetrahedra rotates
14
15 slightly with a resulting decrease in density of SiO_2 .³⁰ During the pyrolysis of the Si-doped char
16
17 at a temperature of 1073 K, the quartz structure should thus change to β -quartz, but change back
18
19 to α -quartz during the subsequent cooling. Some parts of the crystalline structure may be
20
21 preserved in a so-called paramorph state of the β -quartz. The chemisorption of O_2 on β -quartz
22
23 has been reported,³¹ so we hypothesize that hysteresis observed in this work may reflect the
24
25 presence of this β -quartz paramorph in the Si-doped char. However, we have no proof for this
26
27 hypothesis and further verification is necessary, but during several adsorption cycles with the
28
29 same sample, this desorption hysteresis was found to be reproducible.
30
31
32
33
34
35



36
37
38
39
40
41
42
43
44
45
46
47
48
49
50
51
52
53
54
55
56
57
58 **Figure 9.** Adsorption and desorption loadings of O_2 on the undoped (HTC-800), the Si-doped
59 (Si-HTC-800) and the Fe-doped (Fe-HTC-800) HTC chars at (a) $T = 273.15$ K and (b)
60 $T = 298.15$ K. Adsorption plotted by hollowed and desorption by filled symbols.

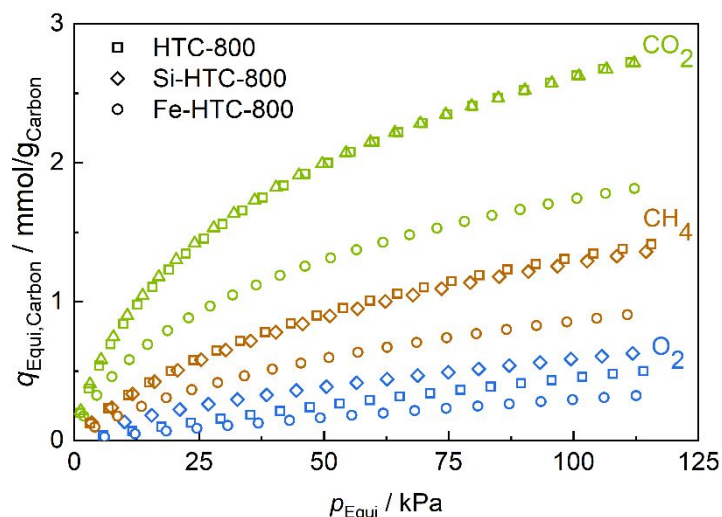


Figure 10. Adsorption loadings of the three gases at $T = 298.15$ K for the undoped (HTC-800), the Si-doped (Si-HTC-800) and the Fe-doped (Fe-HTC-800) HTC char.

To summarize the inhibiting effect of the iron doping on the char adsorption behavior, loadings for each of the three gases at $T = 298.15$ K with regard to the absolute mass of carbon in the chars are shown in Figure 10. For CO_2 and CH_4 , the adsorption loadings on the undoped and the Si-doped chars are essentially the same, while the adsorption on the Fe-doped char is much lower reflecting a clear inhibiting effect by the dopant. For the case of O_2 , the promoting effect of silica can also be observed.

3. CONCLUSIONS

To understand the catalytic influence of minerals in chars, a combined approach to investigate changes of char morphology and adsorption behavior of mineral-doped HTC chars is presented. Different characteristics (XRD, BET, DA and TPO) and the adsorption behavior (CO_2 , CH_4 and O_2 at temperatures between $T = (273.15 - 373.15)$ K) of an undoped, a Si-doped and a Fe-doped char were investigated. The XRD patterns and TEM images show that the Fe-doping increases the structural ordering of the char during pyrolysis, while the Si-doping had no apparent effect on the char structure. BET analysis (N_2 adsorption at $T = 77.36$ K) and Dubinin-Astakhov analysis (CO_2 adsorption at $T = 273.15$ K) showed that the doped chars had smaller macro- and micropore surface areas than the undoped char. While the Fe-doped char had a

1
2
3 larger macropore surface area than the Si-doped char, the opposite was true for the micropore
4 surface areas as a result of the higher fraction of highly ordered domains in the Fe-doped char.
5
6

7
8 For the first time, the influence of mineral doping on the gas adsorption behavior of HTC chars
9 was investigated. The highest adsorption loadings for CO₂ and CH₄ were observed for the
10 undoped char, reflecting its higher microporosity, followed by the Si-doped and the Fe-doped
11 chars. For O₂ adsorption, the highest adsorption affinity was observed for the Si-doped char,
12 which may be explained by chemisorption of O₂ on a paramorph of the doped quartz. Due to
13 less adsorption of all three analysis gases on the Fe-doped char, it can be concluded that Fe
14 doping and the resulting increase in structural order during subsequent pyrolysis leads to less
15 accessible adsorption sites on the surface of the char. The catalytic effect of iron on char
16 conversion is therefore not a consequence of a higher concentration of adsorption sites on the
17 surface. For future research work, the effect of the mineral influence on the rate of pore
18 diffusion has also to be taken into account to reach a complete understanding of the influence
19 on mass transfer.
20
21
22
23
24
25
26
27
28
29
30
31
32
33
34
35
36

37 **4. EXPERIMENTAL METHODS**

38 **4.1. Synthesis of hydrochars**

39
40 Doped synthetic chars were prepared by hydrothermal carbonization (HTC) using cellulose as
41 a precursor followed by pyrolysis of the obtained hydrochars.³² *In situ* doping with SiO₂ or
42 Fe₂O₃ imitated the incorporation of minerals into coal during the natural coalification process.¹²
43
44
45
46
47
48
49

50
51 For the hydrothermal synthesis, a 50 mL polytetrafluoroethylene inliner of a stainless steel
52 autoclave was applied to the reactor. For the undoped hydrochar, 6 g α -cellulose (Sigma
53 Aldrich, BioReagent) was suspended within 30 mL de-ionized H₂O. *In situ* doping was
54 performed by the addition of either 5 wt% Fe₂O₃ (Alfa Aesar, 20-40 nm) or 5 wt% SiO₂
55 (Riedel-de Haën, 40–63 μ m) to the cellulose dispersion. The loaded autoclave was heated in a
56
57
58
59
60

convection oven to $T = 473.15$ K, which generated an autogenous pressure of about 1.55 MPa inside the autoclave. After 24 h, the autoclave was cooled down to room temperature. Subsequently, the yielded suspension was filtered, and the resulting solid was washed with de-ionized H_2O until a neutral pH was reached. The obtained hydrochar was dried in a convection oven at $T = 378.15$ K for 24 h. Afterwards, the hydrochar was loaded into a quartz boat, which was placed in a horizontal oven and pyrolyzed in a N_2 -flow (Air Liquide; purity: 99.999 mol-%) by heating at a linear rate of 5 K min^{-1} to $T = 1073.15$ K, which was then held for 2 h. The resulting undoped, Si-doped and Fe-doped chars are labeled HTC-800, Si-HTC-800 and Fe-HTC-800, respectively.

An overview over the composition of the synthesized and pyrolyzed chars is presented in Table 2. Pyrolysis causes the release of volatiles resulting in an increase of the carbon content accompanied by a decrease of the H and O content in the remaining char. For the undoped char the degree of carbonization was higher than 90 wt%. To specify the extent to which the added dopants were incorporated, the actual loadings are reported as a weight percentage of the particular metal component in the char. The doped amounts correspond to 2.7 wt% Si content for the Si-doped char and 3.8 wt% Fe content for the Fe-doped char. A proximate analysis revealed that the undoped char contained no mineral components in contrast to the doped chars.

Table 2. Overview of characterization of the undoped (HTC-800), the Si-doped (Si-HTC-800) and the Fe-doped (Fe-HTC-800) HTC char by elemental analysis, AAS and proximate analysis.

	HTC-800	Si-HTC-800	Fe-HTC-800
C [wt%]	94.1	84.7	90.6
H [wt%]	0.6	0.8	0.6
O ^{a)} [wt%]	5.3	11.9	5.0
Fe [wt%]	-	-	3.8
Si [wt%]	-	2.7	-
Volatiles [wt%]	4	4	4
Ash [wt%]	0	8	7

4.2. Characterization of chars

The prepared chars were characterized with respect to composition, structural properties and reactivity in an oxidative atmosphere. A vario Micro cube (Elementar Analysensysteme) was used for elemental (CHNS) analysis of the chars. The amount of Si and Fe included in the Si-doped and the Fe-doped char, respectively, was determined by atomic absorption spectroscopy (AAS). For electron microscopy imaging, the doped HTC chars were first suspended in a mixture of ethanol and water and then dispersed in an ultrasonic bath. Afterwards, the samples were placed on an Au grid with a lacey carbon film. Scanning transmission electron microscopy (STEM) and energy-dispersive X-ray (EDX) spectroscopy were performed using a JEOL JEM-2800 microscope. The X-ray diffraction patterns in the 2θ range of 5° to 80° for Cu $K\alpha$ radiation were recorded by an Empyrean diffractometer (Panalytical) at the Department of Mineralogy at Ruhr University Bochum. Phase identification was based on reference patterns by the International Center for Diffraction Data (ICDD), a HighScore Plus software (Malvern Panalytical). The volatile and the ash fractions in the chars were derived from thermogravimetric measurements using a magnetic-suspension balance (TA Instruments, previously Rubotherm) with a coupled quadrupole mass spectrometer (Thermostar, Pfeiffer Vacuum). For proximate analysis, about 30 mg of the carbon materials were heated under a He flow of $100 \text{ cm}^3/\text{min}$ (Air Liquide; purity: 99.999 mol-%) to a temperature of 1173.15 K with a heating rate of 10 K/min followed by treatment at $T = 1088.15 \text{ K}$ in a $100 \text{ cm}^3/\text{min}$ flow of 20/80 vol-% O_2/He (Air Liquide; purities: 99.995 mol-%, 99.999 mol-%). The oxygen content of the chars was calculated by subtraction according to: $\text{O} [\text{wt}\%] = 100 [\text{wt}\%] - \text{C} [\text{wt}\%] - \text{H} [\text{wt}\%] - \text{Si} [\text{wt}\%] - \text{Fe} [\text{wt}\%]$. The influence of the dopants on the stability of the chars was evaluated by temperature-programmed oxidation (TPO) experiments in the magnetic-suspension balance. During TPO, about 30 mg of the chars were heated at 5 K/min to $T = 1173.15 \text{ K}$ in a $100 \text{ cm}^3/\text{min}$ flow of 20/80 vol-% O_2/He .

1
2
3 To determine the meso- to macroporous surface area according to the theory of Brunauer,
4 Emmett and Teller (BET),³³ N₂ (Air Liquide; purity: 99.999 mol-%) adsorption measurements
5
6 at $T = 77.36$ K were carried out in a BELSORP-mini (BEL Japan). Before conducting the
7
8 adsorption measurements, the samples were degassed for 6 h at a temperature of $T = 473.15$ K.
9
10 However, at cryogenic temperatures, the diffusion of N₂ into the HTC char's narrow micropores
11
12 is highly restricted and a quantitative analysis of the sample's microporosity can often not be
13
14 achieved by such measurements.^{34,35} By instead using CO₂ as the adsorbate at $T = 273.15$ K this
15
16 kinetic restriction can be avoided, and given the saturation pressure for CO₂ at this temperature
17
18 is 3.4851 MPa,³⁶ the initial stage of physisorption can be studied at moderate pressures in the
19
20 range (0.1 – 100) kPa.³⁴ However, as CO₂ has a quadrupole moment which can interact with
21
22 functional groups on the char's surface, this could in-principle influence the pore filling.
23
24 Nevertheless, most carbonaceous surfaces in general do not contain as many functional groups
25
26 as e.g. zeolites or MOFs. Furthermore, Lotz *et al.* observed a strong loss of functional groups
27
28 on the hydrochars during pyrolysis. Accordingly, CO₂ was used in this work to analyze the
29
30 microporous structure of the chars^{22,34} using the Dubinin-Astakhov theory with the extended
31
32 equation by Medek.^{23,24} For the CO₂ sorption experiments, the volumetric system described in
33
34 4.3 was used.
35
36
37
38
39
40
41
42

43 The N₂ adsorption data was also used to calculate the pore size distribution by non-linear
44
45 density functional theory (NLDFT) calculations. The 2D-NLDFT model for porous carbons
46
47 with heterogeneous surfaces was used,^{37,38} which is implemented in the analysis software
48
49 *SAIEUS* by Micromeritics.
50
51
52

53 **4.3. Sorption experiments with CO₂, CH₄ and O₂**

54
55
56 For the adsorption investigations, a volumetric measurement system (model ASAP 2020 by
57
58 Micromeritics) was used, which as shown in Figure 11 was slightly modified from its previous
59
60 configurations.^{39–43} The temperature of the solid sample in the measurement cell (marked green

in Figure 11) was controlled by a home-made heating jacket filled with a thermostated heat transfer oil. Temperature and pressure in the manifold volume (marked red in Figure 11) were measured continuously using transducers with full scales and uncertainties shown in Figure 11. After degassing the solid sample at $T = 473.15$ K, the manifold volume was filled with gas up to a certain pressure (e.g. 5 kPa, 10 kPa). Subsequently, valve V13 was opened allowing gas into the measuring cell, and the pressure change associated with adsorption to be determined; after reaching a steady state pressure, the process was repeated multiple times up the isotherm. The CO_2 , O_2 , CH_4 and He were supplied by Coregas with a purity of 99.995 mol-%.

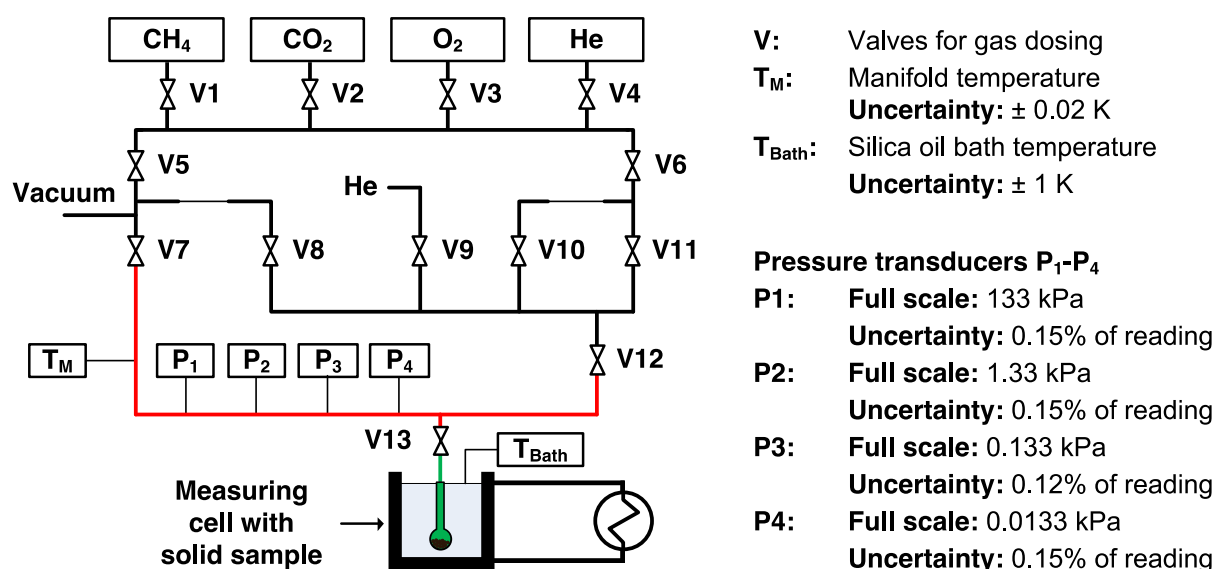


Figure 11. Schematic of the volumetric measurement system.

4.3.1. Experimental procedure

For clarity and to promote a better understanding of the following uncertainty estimation, we briefly present the working equations of the volumetric sorption measurement system. The adsorbed amount at equilibrium is obtained by calculating the difference between the dosed amount n_{dosed} and the amount of gas in the free space n_{FS} inside the measuring volume.

$$n_{\text{equi},i} = n_{\text{dosed},i} - n_{\text{FS},i} \quad (1)$$

The cumulative nature of the measurement requires that the amounts dosed during previous pressure steps have to be account for when evaluating $n_{\text{dosed},i}$. The amount previously dosed is incremented by the difference between the initial and equilibrium amount of gas inside the manifold volume V_M . Real gas behavior is considered using the non-ideality factor α (see Eq. (4)).

$$n_{\text{dosed},i} = n_{\text{dosed},i-1} + \frac{p_{\text{initial}} \cdot V_M}{R \cdot T_{M,\text{initial}}(1 + \alpha \cdot p_{\text{initial}})} - \frac{p_{\text{equi}} \cdot V_M}{R \cdot T_{M,\text{equi}}(1 + \alpha \cdot p_{\text{equi}})} \quad (2)$$

Before starting the adsorption measurement, the free gas volume in the measuring volume is determined twice by helium pycnometry, once at the measurement temperature set by the bath ($V_{\text{FC}}, T_{\text{Bath}}$) and once at room temperature ($V_{\text{FW}}, T_{\text{RM}}$).

$$n_{\text{FS},i} = \frac{p_{\text{Equi}} \cdot V_{\text{FC}}}{R \cdot T_{\text{STD}}(1 + \alpha \cdot p_{\text{equi}})} + \frac{p_{\text{Equi}} \left(V_{\text{FC}} - V_{\text{FW}} \cdot \frac{T_{\text{bath}}}{T_{\text{RM}}} \right)}{R \cdot T_{\text{STD}}(1 + \alpha \cdot p_{\text{equi}})} \quad (3)$$

The non-ideality factor is related to the compressibility factor Z as given in Eq. (4), which depends on the actual temperature and pressure of the gas.⁴⁴ The values^{45,46} for the non-ideality factor still widely used in sorption science are often traceable to the suggestions of Emmett and Brunauer⁴⁷ from 1937. In this work, the far more accurate reference equations of state for CO₂,³⁶ He,⁴⁸ CH₄,⁴⁹ O₂⁵⁰ and N₂⁵¹ were used to calculate Z for different temperatures, using the software package *Trend 4.0*.⁵² Hence, the calculated values for Z and α are listed in

Table 3 and Table 4. These tables also show at which temperature the measurements with the different gases were conducted. CO₂ was measured from $T = 273.15$ K up to $T = 423.15$ K, while CH₄ and O₂ were only measured up to $T = 373.15$ K and $T = 298.15$ K, respectively. At higher temperatures, the experimental loadings of CH₄ and O₂ were so small, that they could not be reproduced properly.

$$\alpha = \frac{Z(T_{\text{bath}}, p_{\text{equi}}) - 1}{p_{\text{equi}}} \quad (4)$$

Table 3. Compressibility factor Z calculated for T and $p_{\text{equi}} = 0.1$ MPa.

	$Z [-]$					
	77.36 K	273.15 K	298.15 K	323.15 K	373.15 K	423.15 K
CO ₂	-	0.99335	0.99502	0.99620	0.99768	0.99853
He	-	1.00053	1.00048	1.00044	1.00037	1.00032
CH ₄	-	0.99764	0.99827	0.99873	0.99932	-
O ₂	-	0.99904	0.99936	-	-	-
N ₂	0.95747	-	-	-	-	-

Table 4. Non-ideality factor α for T and $p_{\text{equi}} = 0.1$ MPa. Note that the *ASAP 2020* device requires α in (*I/Torr*).

	$\alpha [10^{-9}/\text{Pa}]$					
	77.36 K	273.15 K	298.15 K	323.15 K	373.15 K	423.15 K
CO ₂	-	-66.522	-49.793	-38.069	-23.249	-14.699
He	-	5.2618	4.7785	4.3688	3.7138	3.2151
CH ₄	-	-23.561	-17.299	-12.737	-6.7668	-
O ₂	-	-9.5601	-6.3854	-	-	-
N ₂	-425.29	-	-	-	-	-

The adsorption capacity can finally be obtained through the ratio of the adsorbed amount of molecules and the mass of the sample loaded into the measuring cell.

$$q_i = \frac{n_{\text{equi},i}}{m_{\text{Sample}}} \quad (5)$$

4.3.2. Estimation of the volumetric adsorption measurement uncertainty

The measurement uncertainty was estimated according to the “Guide of the Expression of Uncertainty in Measurements”, abbreviated as GUM.⁵³ The combined standard uncertainty u_c of the adsorption capacity q_i can be calculated by Eq. (6) for every single pressure step. Due to the cumulative nature of the measurements, the uncertainties of all previous pressure steps j have to be considered for the uncertainty of the pressure step i ($j = 1$ to i). In Table 5, the standard uncertainties of the different contributions are listed. The standard uncertainties of the pressure and temperature measurements as well of the sample mass determination are taken from the manufacturer specifications. For the volumes, no specifications were provided by the manufacturer of the volumetric measurement system, so we conservatively estimated these

values. The sensitivity coefficients $\partial q_i/\partial x$ were determined by conducting a sensitivity analysis, whereby the influence of the standard uncertainties on the adsorption loading q_i was evaluated. Using a coverage factor of $k = 2$, the combined expanded uncertainty $U_c(q_i)$ in determination of adsorption capacity can be calculated; values are indicated in the figures of section 2.2, and the numerical values are provided as state point uncertainties in the tables of the supporting information.

$$\begin{aligned}
 u_c(q_i) &= \left[\sum_{j=1}^i \left\{ \left(\frac{\partial q_i}{\partial p_{\text{equi},j}} \right) u(p_{\text{equi},j}) \right\}^2 + \left(\frac{\partial q_i}{\partial p_{\text{initial},j}} \right) u(p_{\text{initial},j}) \right]^2 + \left(\frac{\partial q_i}{\partial V_M} \right) u(V_M) \right)^2 \\
 &+ \left(\frac{\partial q_i}{\partial V_{\text{FW}}} \right) u(V_{\text{FW}}) \right)^2 + \left(\frac{\partial q_i}{\partial V_{\text{FC}}} \right) u(V_{\text{FC}}) \right)^2 + \left(\frac{\partial q_i}{\partial T_{\text{bath}}} \right) u(T_{\text{bath}}) \right)^2 + \left(\frac{\partial q_i}{\partial T_{\text{RM}}} \right) u(T_{\text{RM}}) \right)^2 \\
 &+ \left(\frac{\partial q_i}{\partial T_M} \right) u(T_M) \right)^2 + \left(\frac{\partial q_i}{\partial Z} \right) u(Z) \right)^2 + \left(\frac{\partial q_i}{\partial m_{\text{Sample}}} \right) u(m_{\text{Sample}}) \right]^2 \Big]^{0.5} \quad (6)
 \end{aligned}$$

Table 5. Uncertainty budget for the relative combined standard uncertainty in adsorption loading $u_c(q_i)/q_i$ ^{a)}

Uncertainty contribution	Standard uncertainty	Contribution to $u_c(q_i)/q_i$
Equilibrium pressure $p_{\text{equi},i}$	$1.5 \times 10^{-5} p$	2.34×10^{-3}
Initial pressure $p_{\text{initial},i}$	$1.5 \times 10^{-5} p$	2.21×10^{-3}
Manifold volume V_M	$1 \times 10^{-3} V_M$ ^{b)}	1.45×10^{-6}
Free volume at room temperature V_{FW}	$2 \times 10^{-2} V_{\text{FW}}$ ^{c)}	9.70×10^{-8}
Free volume at bath temperature V_{FC}	$2 \times 10^{-2} V_{\text{FC}}$ ^{c)}	9.35×10^{-3}
Bath temperature T_{Bath}	0.5 K	9.53×10^{-10}
Room temperature T_{RM}	0.5 K	1.49×10^{-9}
Manifold temperature T_M	0.02 K	2.94×10^{-4}
Compressibility factor Z	$(0.02 - 0.1) \times 10^{-3} Z$ ^{d)}	3.94×10^{-9}
Mass of sample m_{Sample}	0.0005 g	5.57×10^{-6}
$u_c(q_i)/q_i$	-	1.42×10^{-2}

^{a)} As example, the contributions to $u_c(q_i)/q_i$ were calculated for the adsorption of CO_2 on Si-HTC-800 at $T = 373.15$ K and $p = 110.4$ kPa.

^{b)} Manifold volume was provided by manufacturer, but not the standard uncertainty. Therefore standard uncertainty was conservatively estimated.

^{c)} Free volumes were determined by helium pycnometry before the adsorption measurement started. Since the apparatus routine does not provide the values to recalculate those volumes, standard uncertainties were conservatively estimated.

^{d)} The uncertainty depends on the used EOS for the different fluids.^{36,48–51}

Acknowledgments

This work was funded by the Deutsche Forschungsgemeinschaft (DFG, German Research Foundation) – Projektnummer 215035359 – TRR 129.

Supporting information

TEM micrographs of the undoped and Fe-doped HTC char, Adsorption loadings and their combined expanded uncertainty of CO₂, CH₄ and O₂ on HTC-800, Si-HTC-800 and Fe-HTC-800 at temperatures between 273.15 K and 423.15 K.

References

- (1) Kambo, H. S.; Dutta, A. A comparative review of biochar and hydrochar in terms of production, physico-chemical properties and applications. *Renewable Sustainable Energy Rev.* **2015**, *45*, 359–378.
- (2) Reza, M. T.; Andert, J.; Wirth, B.; Busch, D.; Pielert, J.; Lynam, J. G.; Mumme, J. Hydrothermal Carbonization of Biomass for Energy and Crop Production. *Appl. Bioenergy* **2014**, *1*.
- (3) Liu, Z.; Balasubramanian, R. Upgrading of waste biomass by hydrothermal carbonization (HTC) and low temperature pyrolysis (LTP): A comparative evaluation. *Appl. Energy* **2014**, *114*, 857–864.
- (4) Titirici, M.-M.; White, R. J.; Falco, C.; Sevilla, M. Black perspectives for a green future: hydrothermal carbons for environment protection and energy storage. *Energy Environ. Sci.* **2012**, *5*, 6796.
- (5) Jones, J. M.; Darvell, L. I.; Bridgeman, T. G.; Pourkashanian, M.; Williams, A. An investigation of the thermal and catalytic behaviour of potassium in biomass combustion. *Proc. Combust. Inst.* **2007**, *31*, 1955–1963.
- (6) Trubetskaya, A.; Jensen, P. A.; Jensen, A. D.; Steibel, M.; Spliethoff, H.; Glarborg, P.; Larsen, F. H. Comparison of high temperature chars of wheat straw and rice husk with respect to chemistry, morphology and reactivity. *Biomass Bioenergy* **2016**, *86*, 76–87.
- (7) Khelfa, A.; Sharypov, V.; Fingueneisel, G.; Weber, J. V. Catalytic pyrolysis and gasification of *Miscanthus Giganteus*: Haematite (Fe₂O₃) a versatile catalyst. *J. Anal. Appl. Pyrolysis* **2009**, *84*, 84–88.
- (8) Farrow, T. S.; Sun, C.; Snape, C. E. Impact of biomass char on coal char burn-out under air and oxy-fuel conditions. *Fuel* **2013**, *114*, 128–134.

- 1
2
3 (9) Eom, I.-Y.; Kim, J.-Y.; Kim, T.-S.; Lee, S.-M.; Choi, D.; Choi, I.-G.; Choi, J.-W. Effect of
4 essential inorganic metals on primary thermal degradation of lignocellulosic biomass.
5 *Bioresour. Technol.* **2012**, *104*, 687–694.
6
7
8
9
10 (10) Perander, M.; DeMartini, N.; Brink, A.; Kramb, J.; Karlström, O.; Hemming, J.; Moilanen,
11 A.; Konttinen, J.; Hupa, M. Catalytic effect of Ca and K on CO₂ gasification of spruce wood
12 char. *Fuel* **2015**, *150*, 464–472.
13
14
15
16 (11) Lotz, K.; Berger, C. M.; Muhler, M. Catalytic effect of iron phases on the oxidation of
17 cellulose-derived synthetic char. *Energy Procedia* **2019**, *158*, 694–699.
18
19
20
21 (12) Döder, H.; Wütscher, A.; Vorobiev, N.; Schiemann, M.; Scherer, V.; Muhler, M.
22 Oxidation characteristics of a cellulose-derived hydrochar in thermogravimetric and laminar
23 flow burner experiments. *Fuel Process. Technol.* **2016**, *148*, 85–90.
24
25
26
27 (13) Döder, H.; Lotz, K.; Wütscher, A.; Muhler, M. The influence of iron oxide on the
28 oxidation kinetics of synthetic char derived from thermogravimetric analysis and fixed-bed
29 experiments under isothermal and temperature-programmed conditions. *Fuel* **2017**, *201*, 99–
30 104.
31
32
33
34
35
36
37 (14) Wedler, C.; Richter, M.; Span, R. Integration of sorption kinetics in carbon conversion
38 modeling for the description of oxyfuel combustion processes. *Energy Procedia* **2017**, *142*,
39 1361–1366.
40
41
42
43 (15) Hao, W.; Björkman, E.; Lilliestråle, M.; Hedin, N. Activated carbons prepared from
44 hydrothermally carbonized waste biomass used as adsorbents for CO₂. *Appl. Energy* **2013**, *112*,
45 526–532.
46
47
48
49 (16) Islam, M. A.; Ahmed, M. J.; Khanday, W. A.; Asif, M.; Hameed, B. H. Mesoporous
50 activated coconut shell-derived hydrochar prepared via hydrothermal carbonization-NaOH
51 activation for methylene blue adsorption. *J. Environ. Manage.* **2017**, *203*, 237–244.
52
53
54
55
56
57
58
59
60

1
2
3 (17) Sevilla, M.; Maciá-Agulló, J. A.; Fuertes, A. B. Hydrothermal carbonization of biomass
4 as a route for the sequestration of CO₂: Chemical and structural properties of the carbonized
5 products. *Biomass Bioenergy* **2011**, *35*, 3152–3159.
6
7

8
9
10 (18) Sun, K.; Ro, K.; Guo, M.; Novak, J.; Mashayekhi, H.; Xing, B. Sorption of bisphenol A,
11 17 α -ethinyl estradiol and phenanthrene on thermally and hydrothermally produced biochars.
12 *Bioresour. Technol.* **2011**, *102*, 5757–5763.
13
14

15
16
17 (19) Yang, G.; Song, S.; Li, J.; Tang, Z.; Ye, J.; Yang, J. Preparation and CO₂ adsorption
18 properties of porous carbon by hydrothermal carbonization of tree leaves. *J. Mater. Sci.*
19 *Technol.* **2019**, *35*, 875–884.
20
21

22
23
24 (20) Yu, J.; Zhu, Z.; Zhang, H.; Chen, T.; Qiu, Y.; Xu, Z.; Yin, D. Efficient removal of several
25 estrogens in water by Fe-hydrochar composite and related interactive effect mechanism of
26 H₂O₂ and iron with persistent free radicals from hydrochar of pinewood. *Sci. Total Environ.*
27 **2019**, *658*, 1013–1022.
28
29

30
31
32 (21) Lei, Y.; Su, H.; Tian, F. A Novel Nitrogen Enriched Hydrochar Adsorbents Derived from
33 Salix Biomass for Cr (VI) Adsorption. *Sci. Rep.* **2018**, *8*, 4040.
34
35

36
37 (22) Lotz, K.; Wütscher, A.; Düdler, H.; Berger, C. M.; Russo, C.; Mukherjee, K.; Schwaab,
38 G.; Havenith, M.; Muhler, M. Tuning the Properties of Iron-Doped Porous Graphitic Carbon
39 Synthesized by Hydrothermal Carbonization of Cellulose and Subsequent Pyrolysis. *ACS*
40 *Omega* **2019**, *4*, 4448–4460.
41
42
43
44

45
46 (23) Dubinin, M. M.; Astakhov, V. A. Development of the concepts of volume filling of
47 micropores in the adsorption of gases and vapors by microporous adsorbents: Communication
48 1. Carbon adsorbents. *Russ. Chem. Bull.* **1971**, *20*, 3–7.
49
50
51

52
53 (24) Medek, J. Possibility of micropore analysis of coal and coke from the carbon dioxide
54 isotherm. *Fuel* **1977**, *56*, 131–133.
55
56

57
58 (25) Henrich, E.; Bürkle, S.; Meza-Renken, Z.I.; Rumpel, S. Combustion and gasification
59 kinetics of pyrolysis chars from waste and biomass. *J. Anal. Appl. Pyrolysis* **1999**, *49*, 221–241.
60

1
2
3 (26) Qian, L.; Zhao, Y.; Sun, S.; Che, H.; Chen, H.; Wang, D. Chemical/physical properties of
4 char during devolatilization in inert and reducing conditions. *Fuel Process. Technol.* **2014**, *118*,
5 327–334.
6
7

8
9
10 (27) Wedler, C.; Arami-Niya, A.; Xiao, G.; Span, R.; May, E. F.; Richter, M. Gas Diffusion
11 and Sorption in Carbon Conversion. *Energy Procedia* **2019**, *158*, 1792–1797.
12
13

14 (28) Himeno, S.; Komatsu, T.; Fujita, S. High-Pressure Adsorption Equilibria of Methane and
15 Carbon Dioxide on Several Activated Carbons. *J. Chem. Eng. Data* **2005**, *50*, 369–376.
16
17

18 (29) An, F.-H.; Cheng, Y.-P.; Wu, D.-M.; Wang, L. The effect of small micropores on methane
19 adsorption of coals from Northern China. *Adsorption* **2013**, *19*, 83–90.
20
21
22

23 (30) Borchardt-Ott, W. *Crystallography: An Introduction*; Springer-Verlag Berlin Heidelberg:
24 Berlin, Heidelberg, 2012.
25
26

27 (31) Zazza, C.; Rutigliano, M.; Sanna, N.; Barone, V.; Cacciatore, M. Oxygen adsorption on
28 β -quartz model surfaces: some insights from density functional theory calculations and
29 semiclassical time-dependent dynamics. *J. Phys. Chem. A* **2012**, *116*, 1975–1983.
30
31
32
33

34 (32) Düdder, H.; Wütscher, A.; Stoll, R.; Muhler, M. Synthesis and characterization of lignite-
35 like fuels obtained by hydrothermal carbonization of cellulose. *Fuel* **2016**, *171*, 54–58.
36
37
38

39 (33) Brunauer, S.; Emmett, P. H.; Teller, E. Adsorption of gases in multimolecular layers. *J.*
40 *Am. Chem. Soc.* **1938**, *60*, 309–319.
41
42
43

44 (34) Thommes, M.; Kaneko, K.; Neimark, A. V.; Olivier, J. P.; Rodriguez-Reinoso, F.;
45 Rouquerol, J.; Sing, K. S.W. Physisorption of gases, with special reference to the evaluation of
46 surface area and pore size distribution (IUPAC Technical Report). *Pure Appl. Chem.* **2015**, *87*,
47 1051–1069.
48
49
50
51

52 (35) Garrido, J.; Linares-Solano, A.; Martin-Martinez, J. M.; Molina-Sabio, M.; Rodriguez-
53 Reinoso, F.; Torregrosa, R. Use of nitrogen vs. carbon dioxide in the characterization of
54 activated carbons. *Langmuir* **1987**, *3*, 76–81.
55
56
57
58
59
60

- 1
2
3 (36) Span, R.; Wagner, W. A New Equation of State for Carbon Dioxide Covering the Fluid
4 Region from the Triple-Point Temperature to 1100 K at Pressures up to 800 MPa. *J. Phys.*
5 *Chem. Ref. Data* **1996**, *25*, 1509–1596.
6
7
8
9
10 (37) Jagiello, J.; Olivier, J. P. Carbon slit pore model incorporating surface energetical
11 heterogeneity and geometrical corrugation. *Adsorption* **2013**, *19*, 777–783.
12
13
14 (38) Jagiello, J.; Olivier, J. P. 2D-NLDFT adsorption models for carbon slit-shaped pores with
15 surface energetical heterogeneity and geometrical corrugation. *Carbon* **2013**, *55*, 70–80.
16
17
18 (39) Jensen, N. K.; Rufford, T. E.; Watson, G.; Zhang, D. K.; Chan, K. I.; May, E. F. Screening
19 Zeolites for Gas Separation Applications Involving Methane, Nitrogen, and Carbon Dioxide. *J.*
20 *Chem. Eng. Data* **2012**, *57*, 106–113.
21
22
23
24 (40) Li, G. K.; Shang, J.; Gu, Q.; Awati, R. V.; Jensen, N.; Grant, A.; Zhang, X.; Sholl, D. S.;
25 Liu, J. Z.; Webley, P. A.; *et al.* Temperature-regulated guest admission and release in
26 microporous materials. *Nat. Commun.* **2017**, *8*, 15777.
27
28
29
30
31
32 (41) Rufford, T. E.; Watson, G. C. Y.; Saleman, T. L.; Hofman, P. S.; Jensen, N. K.; May, E.
33 F. Adsorption Equilibria and Kinetics of Methane + Nitrogen Mixtures on the Activated Carbon
34 Norit RB3. *Ind. Eng. Chem. Res.* **2013**, *52*, 14270–14281.
35
36
37
38 (42) Watson, G. C.; Jensen, N. K.; Rufford, T. E.; Chan, K. I.; May, E. F. Volumetric
39 Adsorption Measurements of N₂, CO₂, CH₄, and a CO₂ + CH₄ Mixture on a Natural
40 Chabazite from (5 to 3000) kPa. *J. Chem. Eng. Data* **2012**, *57*, 93–101.
41
42
43
44 (43) Xiao, G.; Li, Z.; Saleman, T. L.; May, E. F. Adsorption equilibria and kinetics of CH₄ and
45 N₂ on commercial zeolites and carbons. *Adsorption* **2017**, *23*, 131–147.
46
47
48
49 (44) Venkatraman, A.; Fan, L. T.; Walawender, W. P. Nonideality Correction Factors for
50 Adsorbates. *J. Colloid Interface Sci.* **1996**, *183*, 291–294.
51
52
53
54 (45) Hallmann, S.; Fink, M. J.; Mitchell, B. S. Wetting properties of silicon films from alkyl-
55 passivated particles produced by mechanochemical synthesis. *J. Colloid Interface Sci.* **2010**,
56 *348*, 634–641.
57
58
59
60

1
2
3 (46) Shaikh, R. P.; Pillay, V.; Choonara, Y. E.; Du Toit, L. C.; Ndesendo, V. M. K.; Kumar,
4 P.; Khan, R. A. The application of a crosslinked pectin-based wafer matrix for gradual buccal
5 drug delivery. *J. Biomed. Mater. Res., Part B* **2012**, *100*, 1029–1043.
6
7

8
9
10 (47) Emmett, P. H.; Brunauer, S. The Use of Low Temperature van der Waals Adsorption
11 Isotherms in Determining the Surface Area of Iron Synthetic Ammonia Catalysts. *J. Am. Chem.*
12 *Soc.* **1937**, *59*, 1553–1564.
13
14

15
16 (48) Ortiz-Vega, D. O.; Hall, K. R.; Holste, J. C.; Arp, V. D.; Harvey, A. H.; Lemmon, E. W.
17 Helmholtz equation of state for helium. *to be published in J. Phys. Chem. Ref. Data* **2020**.
18
19

20
21 (49) Setzmann, U.; Wagner, W. A New Equation of State and Tables of Thermodynamic
22 Properties for Methane Covering the Range from the Melting Line to 625 K at Pressures up to
23 100 MPa. *J. Phys. Chem. Ref. Data* **1991**, *20*, 1061–1155.
24
25

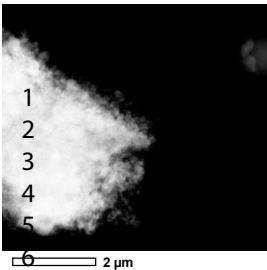
26
27 (50) Stewart, R. B.; Jacobsen, R. T.; Wagner, W. Thermodynamic Properties of Oxygen from
28 the Triple Point to 300 K with Pressures to 80 MPa. *J. Phys. Chem. Ref. Data* **1991**, *20*, 917–
29 1021.
30
31

32
33 (51) Span, R.; Lemmon, E. W.; Jacobsen, R. T.; Wagner, W.; Yokozeki, A. A Reference
34 Equation of State for the Thermodynamic Properties of Nitrogen for Temperatures from 63.151
35 to 1000 K and Pressures to 2200 MPa. *J. Phys. Chem. Ref. Data* **2000**, *29*, 1361–1433.
36
37

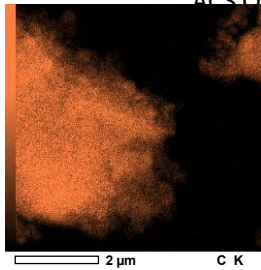
38
39 (52) Span, R.; Beckmüller, R.; Eckermann, T.; Herrig, S.; Hielscher, S.; Jäger, A.; Mickoleit,
40 E.; Neumann, T.; Pohl, S.; Semrau, B.; *et al.* *TREND. Thermodynamic Reference and*
41 *Engineering Data*; Lehrstuhl für Thermodynamik, Ruhr-Universität Bochum, 2019.
42
43

44
45 (53) International Organization for Standardization. *ISO/IEC Guide 98–3:2008: Uncertainty*
46 *of measurement - Part 3: Guide to the expression of uncertainty in measurement*; Geneva, 2008.
47
48
49
50
51
52
53
54
55
56
57
58
59
60

(a)

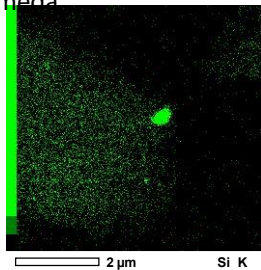


(b)

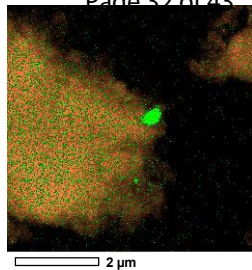


ACS Omega

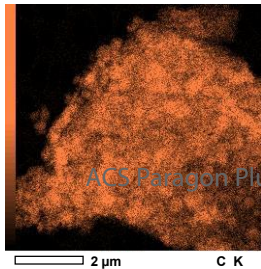
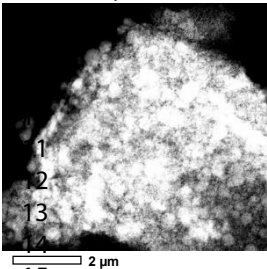
(c)



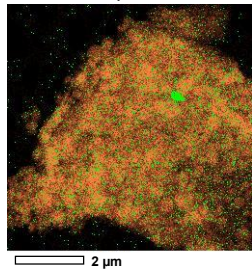
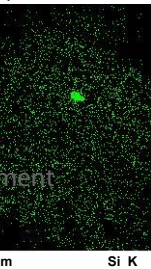
(d)



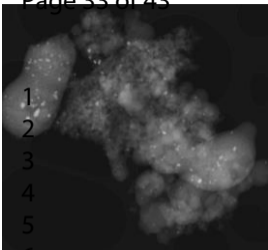
Page 32 of 43



ACS Paragon Plus Environment

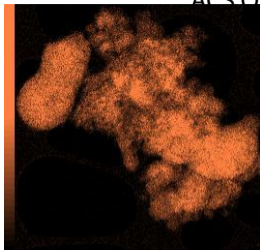


(a)

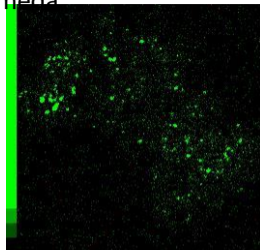


(b)

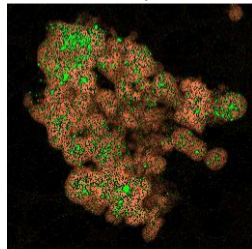
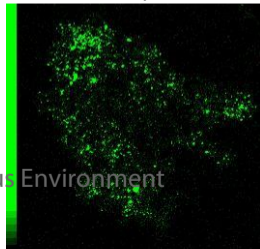
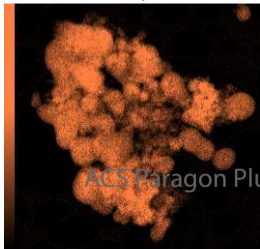
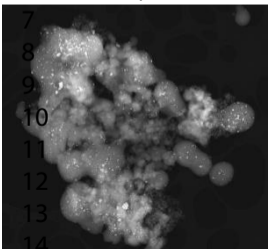
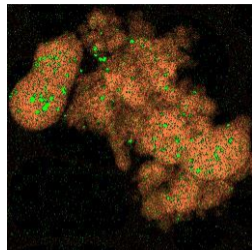
ACS Omega



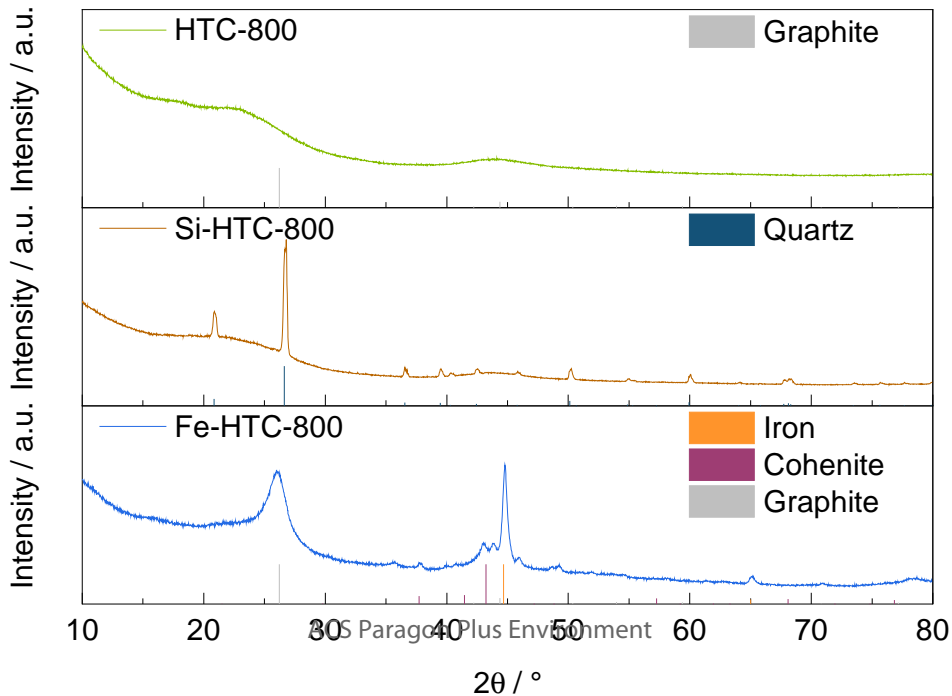
(c)

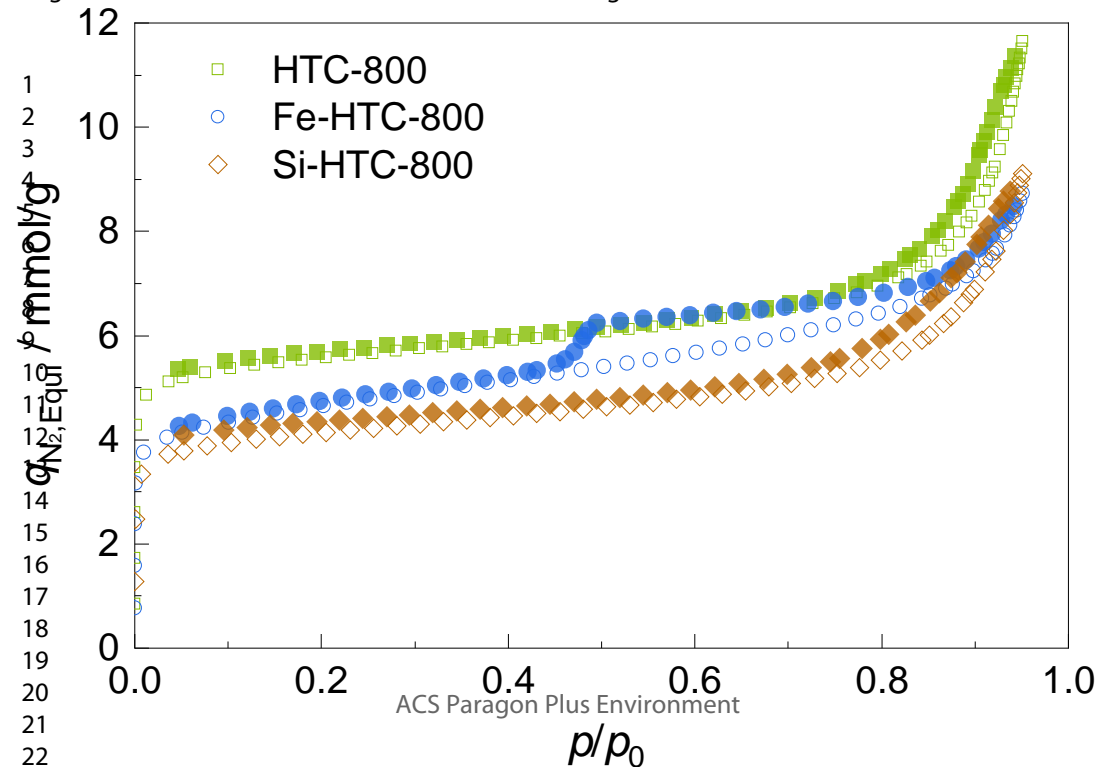


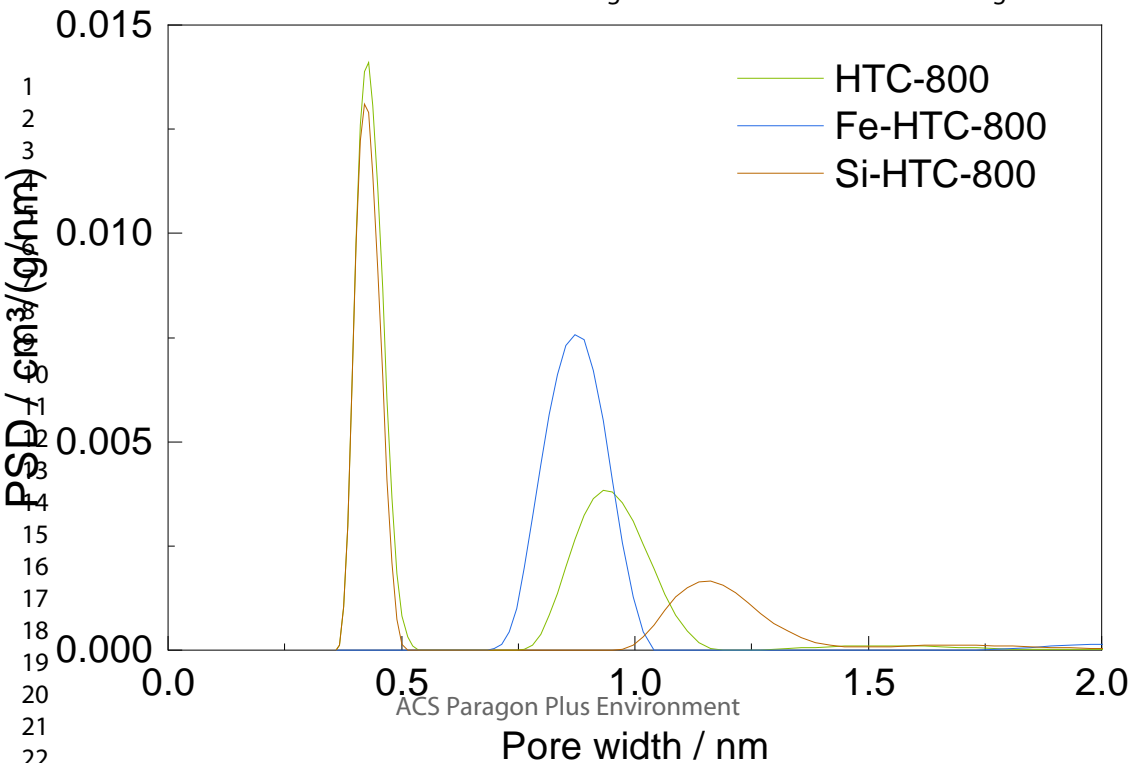
(d)

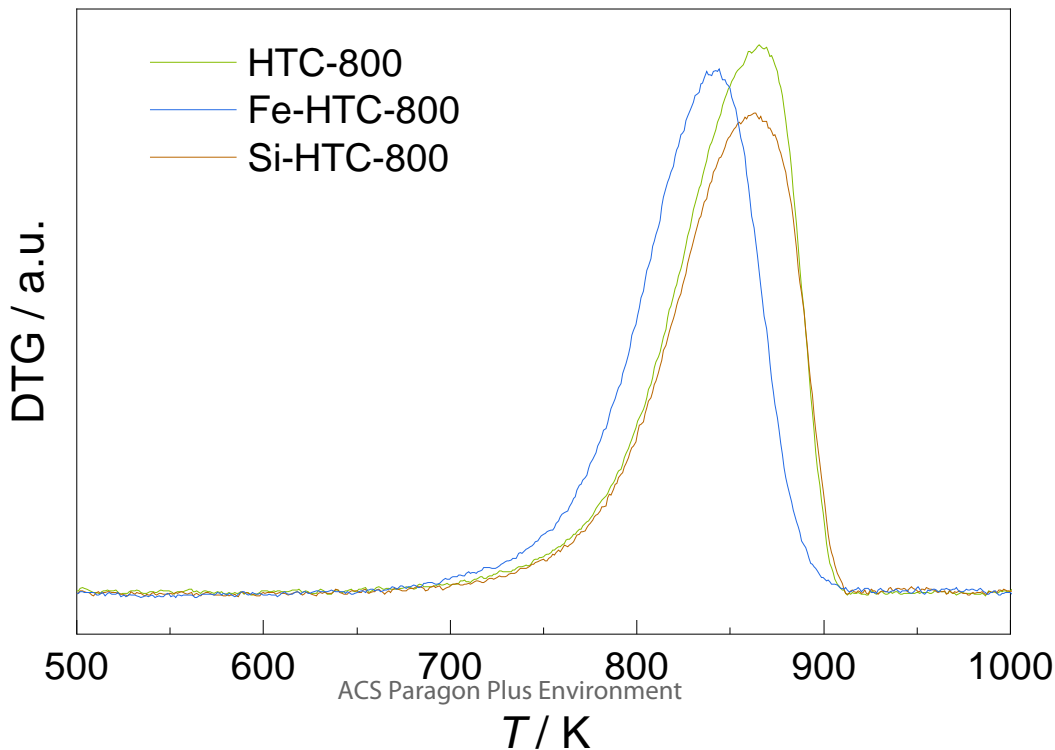


ACS Paragon Plus Environment

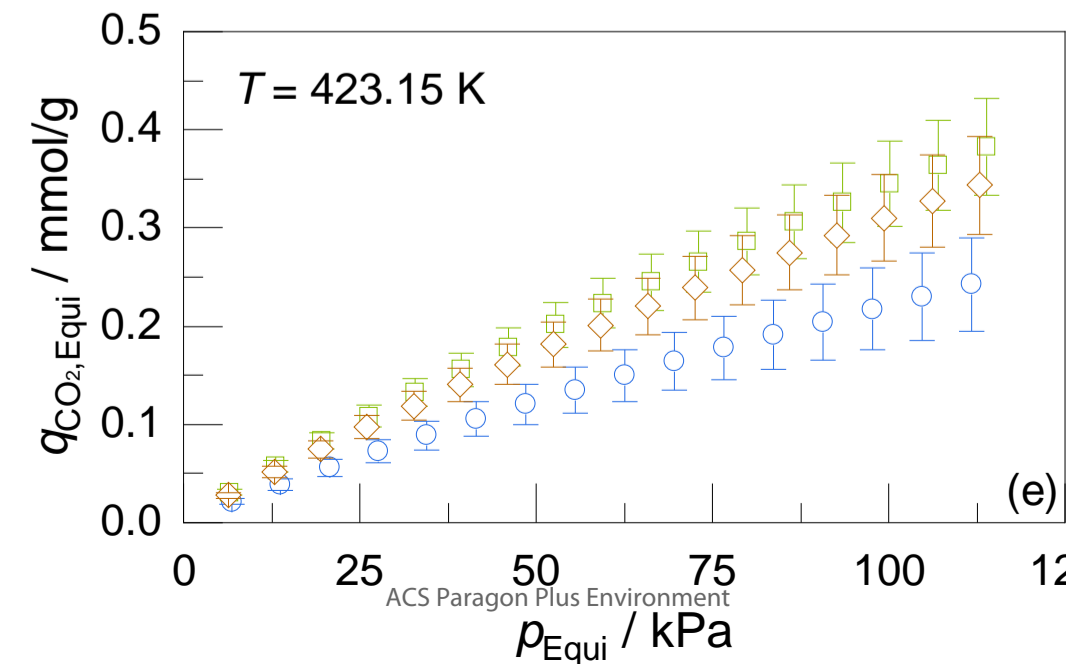
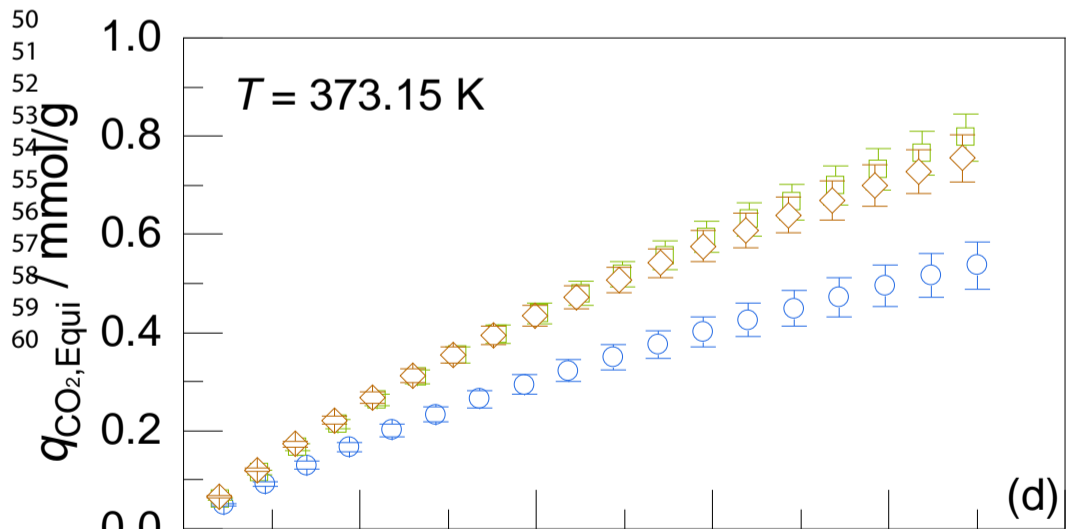
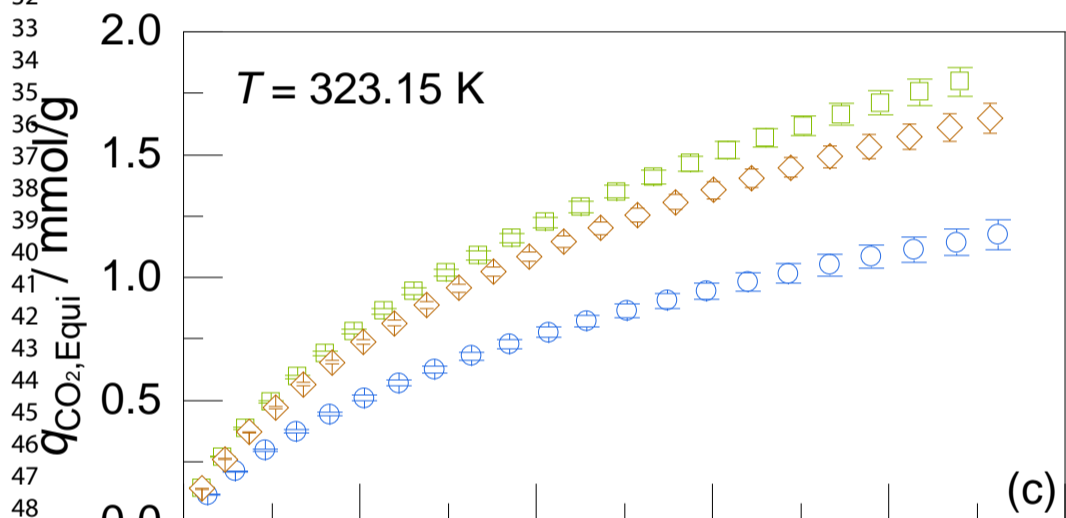
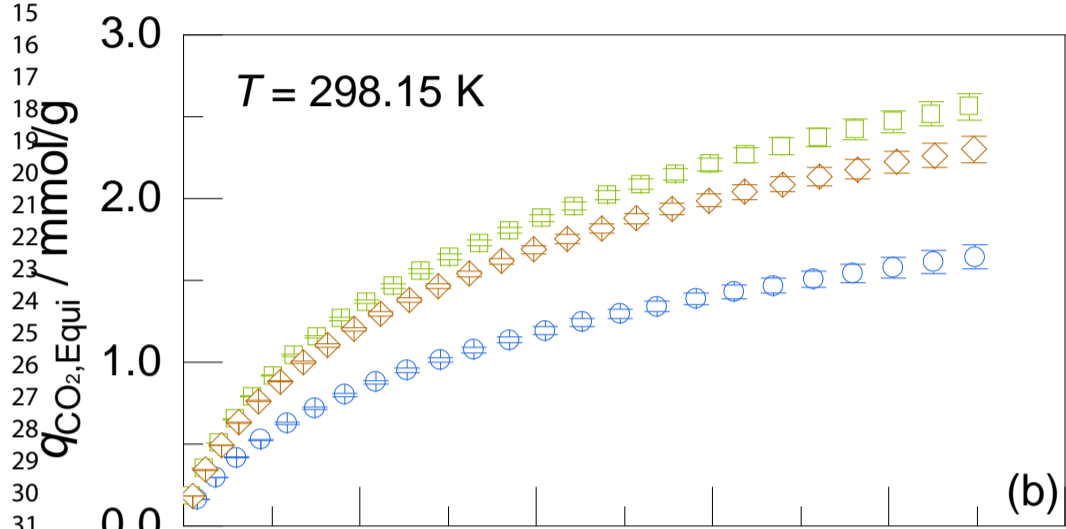
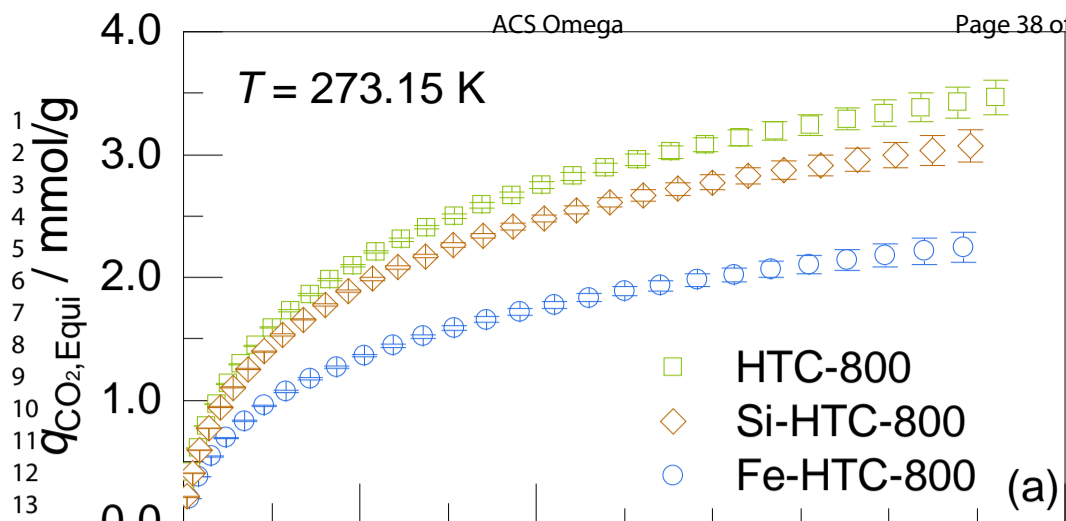


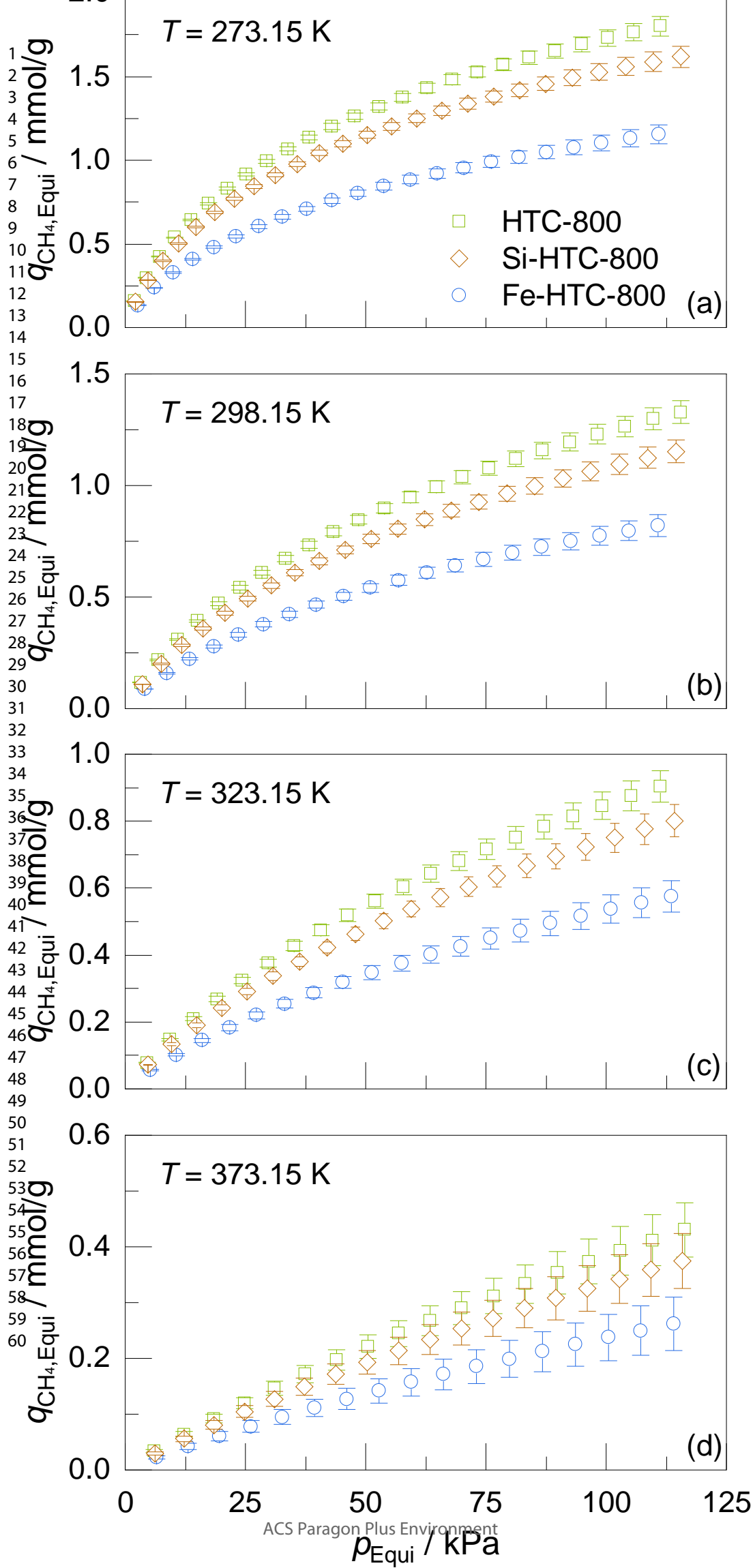


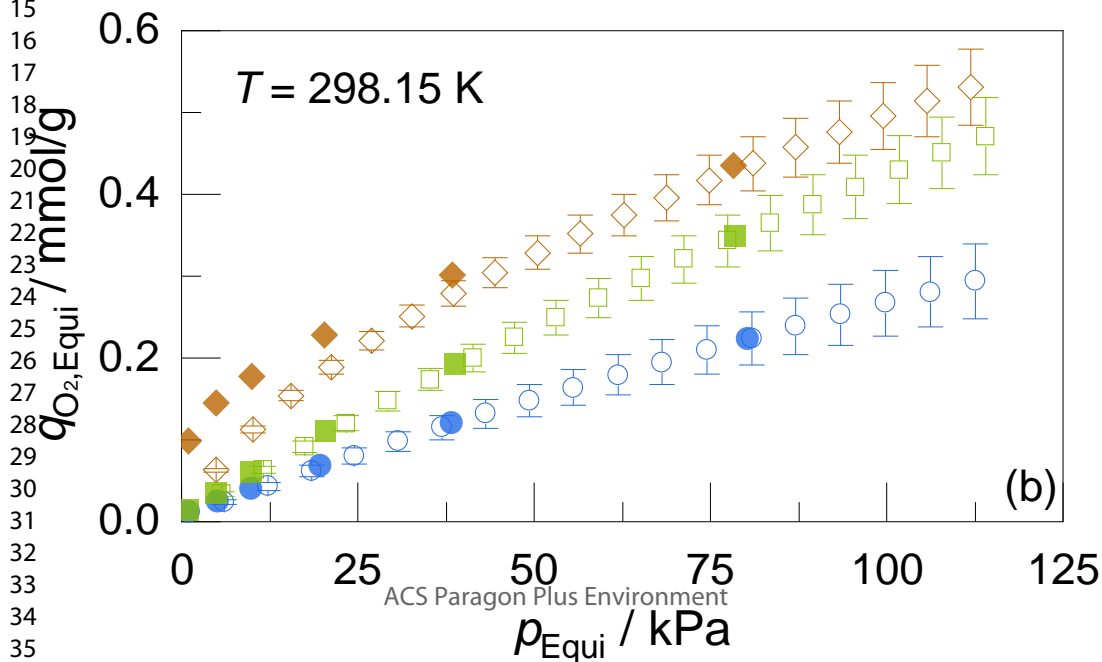
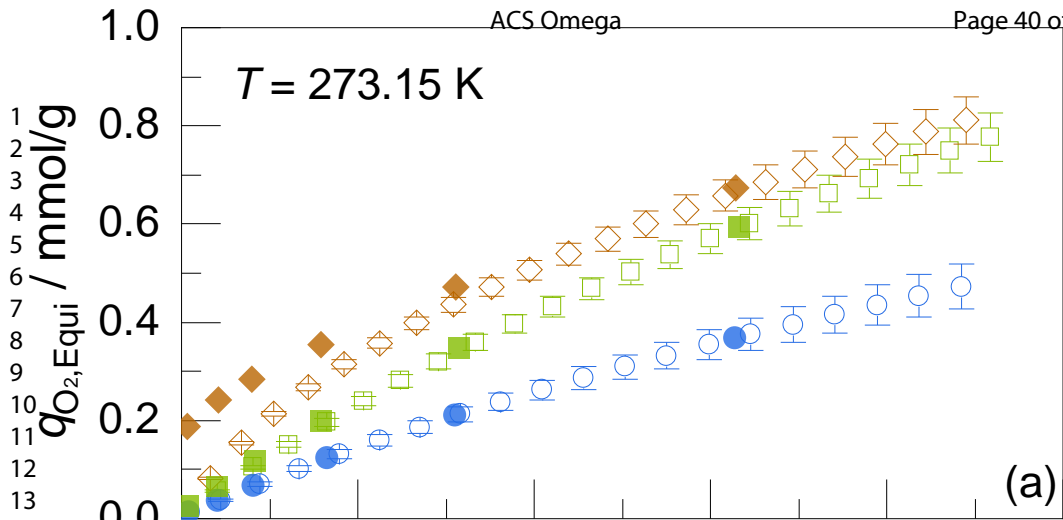


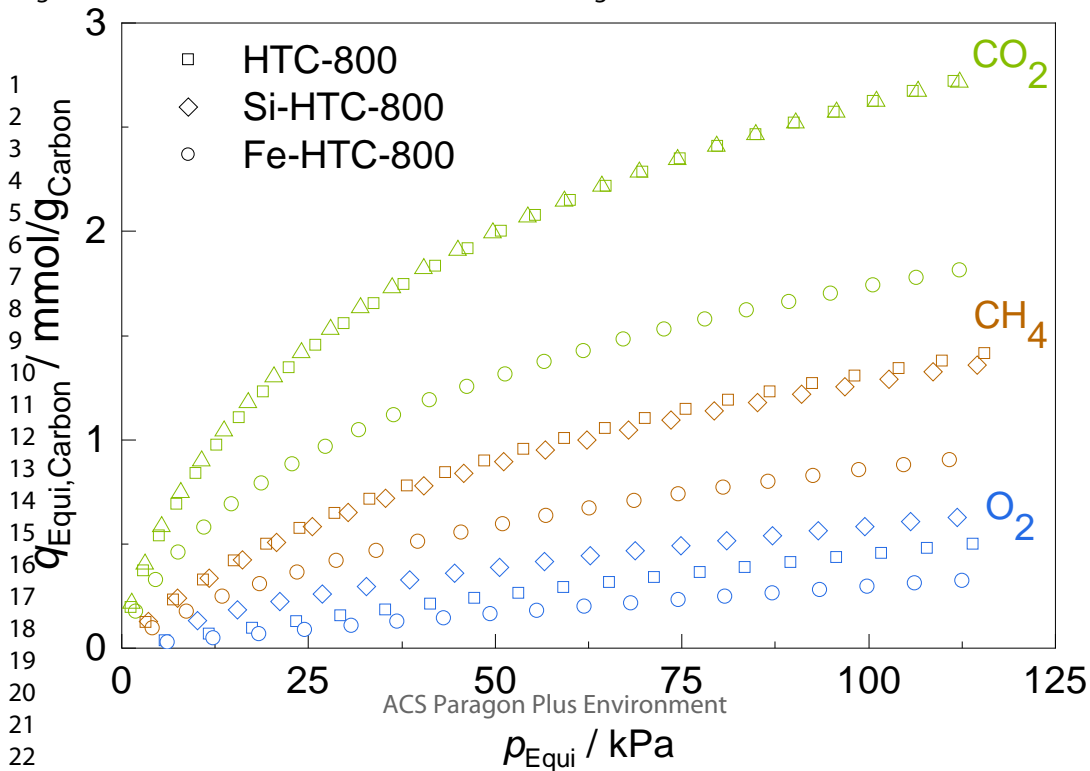
1
2
3
4
5
6
7
8
9
10
11
12
13
14
15
16
17
18
19
20
21
22
23

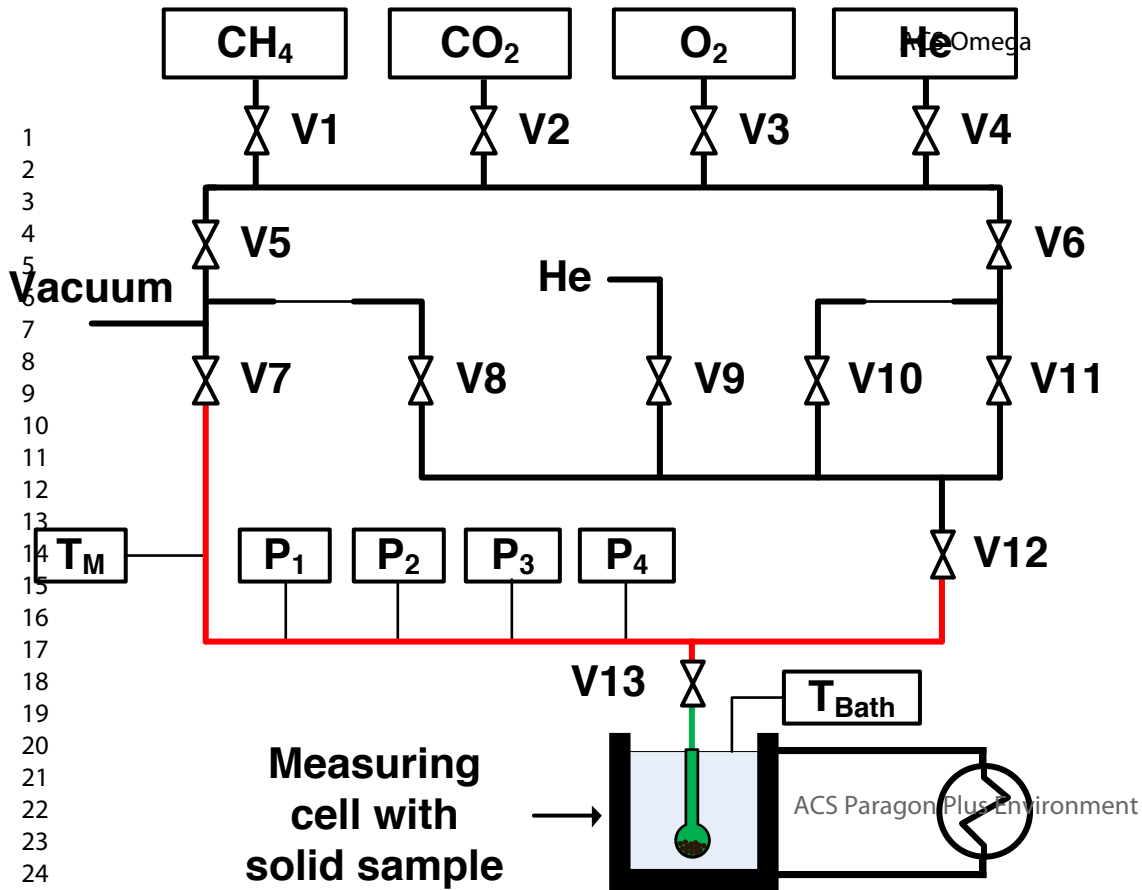
ACS Paragon Plus Environment











V: Valves for gas dosing

T_M: Manifold temperature

Uncertainty: ± 0.02 K

T_{Bath}: Silica oil bath temperature

Uncertainty: ± 1 K

Pressure transducers P₁-P₄

P1: Full scale: 133 kPa

Uncertainty: 0.15% of reading

P2: Full scale: 1.33 kPa

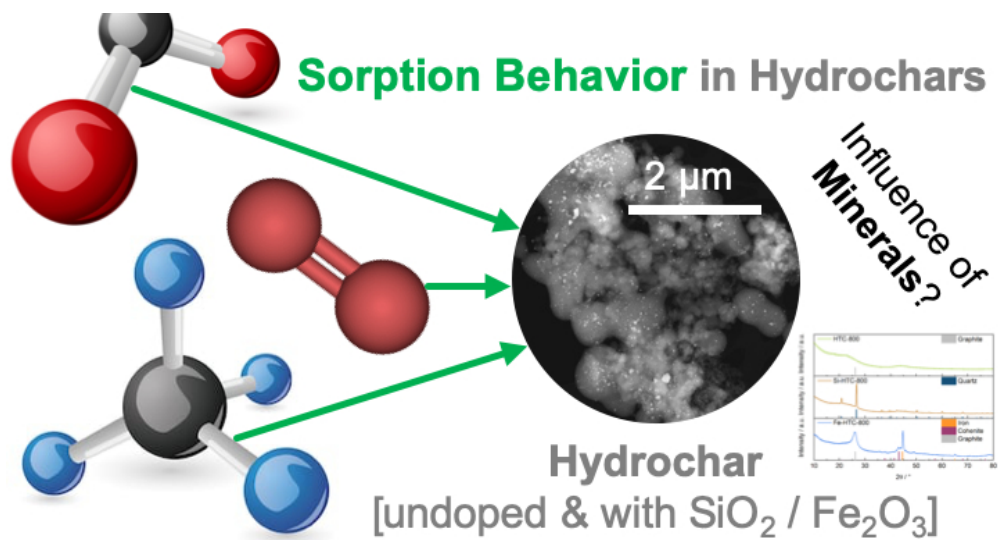
Uncertainty: 0.15% of reading

P3: Full scale: 0.133 kPa

Uncertainty: 0.12% of reading

P4: Full scale: 0.0133 kPa

Uncertainty: 0.15% of reading



82x43mm (223 x 223 DPI)